RESOLVING THE HIGH ENERGY UNIVERSE WITH STRONG GRAVITATIONAL LENSING:
THE CASE OF PKS 1830-211

Anna Barnacka[1,2], Margaret J. Geller[1], Ian P. Dell'Antonio[3], and Wystan Benbow[1]

[1]Harvard-Smithsonian Center for Astrophysics, 60 Garden St, MS-20, Cambridge, MA 02138, USA
[2]Astronomical Observatory, Jagiellonian University, Cracow, Poland
[3]Department of Physics, Brown University, Box 1843, Providence, RI 02912

## ABSTRACT

Gravitational lensing is a potentially powerful tool for elucidating the origin of gamma-ray emission from distant sources. Cosmic lenses magnify the emission from distance sources and produce time delays between mirage images. Gravitationally-induced time delays depend on the position of the emitting regions in the source plane. The *Fermi*/LAT satellite continuously monitors the entire sky and detects gamma-ray flares, including those from gravitationally-lensed blazars. Therefore, temporal resolution at gamma-ray energies can be used to measure these time delays, which, in turn, can be used to resolve the origin of the gamma-ray flares spatially. We provide a guide to the application and Monte Carlo simulation of three techniques for analyzing these unresolved light curves: the Autocorrelation Function, the Double Power Spectrum, and the Maximum Peak Method. We apply these methods to derive time delays from the gamma-ray light curve of the gravitationally-lensed blazar PKS 1830-211. The result of temporal analysis combined with the properties of the lens from radio observations yield an improvement in spatial resolution at gamma-ray energies by a factor of 10000. We analyze four active periods. For two of these periods, the emission is consistent with origination from the core and for the other two, the data suggest that the emission region is displaced from the core by more that $\sim 1.5$ kpc. For the core emission, the gamma-ray time delays, $23 \pm 0.5$ days and $19.7 \pm 1.2$ days, are consistent with the radio time delay $26^{+4}_{-5}$ days.

*Subject headings:* Galaxies: active – gravitational lensing: strong –gamma-rays: jets –methods: signal processing

### 1. INTRODUCTION

Our ability to study gamma-ray radiation from distant sources is observationally limited by the poor ($\sim 0.1°$) angular resolution of the detectors. We demonstrate a technique for using a cosmic lens to enhance the angular resolution at gamma-ray energies.

#### 1.1. *History and Challenges*

The high-energy sky is dominated by the most extreme and puzzling objects in the universe. These sources harbor powerful jets, the largest particle accelerators in the universe; they produce radiation ranging from radio wavelengths up to very high-energy gamma rays. Observations of jets, from radio to X-ray wavelengths, where the sources are resolved, reveal very complex structures including bright knots, blobs and filaments with sizes ranging from subparsecs up to dozens of kpcs (Biretta et al. 1991; Siemiginowska et al. 2002; Marshall et al. 2005; Harris & Krawczynski 2006; Tavecchio et al. 2007; Marscher et al. 2008). Observations with improved angular resolution have revealed that the variability of these sources can be very complex; the flaring emission can originate from regions close to the core, or it can originate from knots along the jet, as in M87 (Harris et al. 2006).

At gamma-ray energies, the *Fermi*/LAT satellite continuously detects flares from hundreds of blazars. *Fermi*/LAT scans the entire sky in a few hours and thus

abarnacka@cfa.harvard.edu

the time resolutions for any well-detected source is excellent. However, the angular resolution of *Fermi*/LAT is at best $\sim 0.1°$, precluding localization of the flares along the jets, even for nearby sources. To resolve gamma-ray emission from even M87, an improvement in angular resolution by a factor of 1000 is required. The angular resolution of gamma-ray detectors is strongly limited by physical effects, such as nuclear recoil, and is unlikely to improve by more than a factor of a few in future instruments (Bernard et al. 2014; Wu et al. 2014).

Jets can be well resolved in the radio band down to sub parsec scales. The variability time scales at radio wavelengths are large, weeks to months, compared to gamma-ray time scales of hours to days. Radio monitoring shows that roughly 2/3 of the gamma-ray flares coincide with the appearance of a new superluminal knot and/or a flare in the millimeter-wave core located parsecs from the central engine (Marscher et al. 2010; Agudo et al. 2011; Marscher et al. 2012; Marscher 2012; Fuhrmann et al. 2014; Ramakrishnan et al. 2014).

Further study shows correlations and similarities between multiwavelength and gamma-ray observations (León-Tavares et al. 2012; Chatterjee et al. 2012; Sandrinelli et al. 2014). However, Max-Moerbeck et al. (2014) modeled the light curves of blazars as red noise processes, and found that only 1 of 41 sources with high-quality data in both the radio and gamma-ray bands shows correlations with a significance larger than $3\sigma$. They thus demonstrate the difficulties of measuring statistically robust multiwavelength correlations even when the data span many years.

## 1.2. *The Importance of the Spatial Origin of Flares*

The origin of gamma-ray flares is a subject of intense debate (Nalewajko et al. 2014a; Tavecchio et al. 2010). In theoretical modeling, it is generally assumed that gamma-ray flares originate from regions close to the central engine, typically on parsec scales (Nalewajko et al. 2014b; Barnacka et al. 2014c; Nalewajko et al. 2014a; Hovatta et al. 2015; Tanaka et al. 2011). However, detailed X-ray observations of M87 have revealed that powerful flares can originate from distant knots along the jet, hundreds of parsecs from the central engine (Harris et al. 2003). The intrinsic complexity of these sources has implications for the physical radiation mechanisms and it introduces potential systematic issues in the use of these sources as cosmological probes.

Models where the high energy emission occurs close to the base of the jet and one where it originates from spatially distinct knots, as in M87, differ in the underlying fundamental physics (Dermer et al. 1992; Bloom & Marscher 1996; Sikora et al. 1994, 2013, 2009; Giannios et al. 2009; Mücke et al. 2003; Böttcher et al. 2013; Reimer et al. 2004; Stawarz et al. 2005, 2006; Meyer & Georganopoulos 2014). Thus, the location of gamma-ray flares is crucial for understanding particle acceleration and magnetic fields at both small and large distances from massive black holes.

Multiple variable emitting regions place limitations on the use of the most variable quasars for measurement of the Hubble parameter based on time delays. Barnacka et al. (2015) point out that even a small spatial offset, for example 5% of Einstein radius, between the resolved position of the core and site of variable emission may result in a bimodal distribution of values of Hubble parameters characterized by an RMS of $\sim 12\,[\mathrm{km\,s^{-1}\,Mpc^{-1}}]$. Complex structure can be an important source of systematics in measurement of the Hubble parameter from gravitationally induced time delays.

## 1.3. *Gravitational Lensing as a High Resolution Cosmic Telescope*

Cosmic lenses magnify light of distant sources and produce delayed mirage images of the emitting regions. The time delay and magnification ratio between mirage images depend on the position of the emitting region in the source plane and the mass distribution of the lens. The properties of the lens are constrained by lens modeling based on resolved radio and optical images. For lenses at a low enough redshift, the velocity dispersion of the lens can be measured, allowing for independent constraints on the mass of the lens (Bolton et al. 2008).

Time delays and magnification ratios derived from well-sampled light curves can elucidate the location of the emitting region. Barnacka et al. (2014b) built a toy model placing an M87 analog at $z \sim 1$, with a galaxy acting as a lens at $z \sim 0.6$. In the M87 case, the projected distance between the core and the flaring knot HST1 is 60 pc (Biretta et al. 1991) or in the toy model $\sim 3\%$ of the Einstein radius. In the toy model, the differences in time delay ($\sim 3$ days) and magnification ratio ($\sim 0.2$) resulting from displacement of the radiation source to the jet location can be measured with current instruments. Thus cosmic lenses are, in principle, a tool for revealing the origin of gamma-ray flares once the time delays are measured.

Measurement of the time delays from unresolved light curves requires long, evenly-sampled time series with low photon noise. Thanks to the *Fermi*/LAT observation strategy, the light curves are perfectly suited for these time delay measurements. Thus, the temporal resolution of the *Fermi*/LAT satellite translates into spatial resolution with the help of cosmic lenses.

## 1.4. *Outline*

We use PKS 1830-211 as a prototypical example of a gravitationally-lensed, gamma-ray emitting system (Section 2.1;Section 2.2). Our ability to resolve the gamma-ray sky relies on time delay measurement (Section 3). We evaluate our methods with Monte Carlo simulations (Section 3.1). We characterize the signal in Section 3.1.1, and evaluate the probability of detecting gravitationally-induced time delays and distinguishing them from spurious fluctuations in the power law noise using approaches described in Sections 3.1.2 and 3.1.3.

We use three methods of time delay estimation. We start with the most commonly used Autocorrelation Function (Section 3.2.1). We describe the details of the Double Power Spectrum method in Section 3.2.2 and demonstrate the steps and importance of signal processing in Appendix A. We also develop the Maximum Peak Method (Section 3.2.3) and evaluate it with Monte Carlo simulations in Appendix B.

We analyze four series of gamma-ray flares in Sections 4.1, 4.2, 4.3, and 4.4. We use the time delays and properties of the lens to elucidate the origin of these flares which we discuss in Section 5, and we conclude in Section 6.

## 2. PKS 1830-211

PKS 1830-211 is a bright blazar lensed by a galaxy located close to the line-of-sight. The emission from PKS 1830-211 is detected across almost the entire electromagnetic spectrum, from radio up to gamma rays. In section 2.1, we describe the gravitationally-lensed system and, in section 2.2, we detail the gamma-ray emission as observed by the Fermi satellite over a 6.5-year period.

## 2.1. *PKS 1830-211 as Gravitationally-Lensed System*

Pramesh Rao & Subrahmanyan (1988) first recognized PKS 1830-211 as a gravitationally-lensed quasi-stellar object. The lens is a face-on spiral galaxy at redshift $z = 0.886$ (Wiklind & Combes 1996, 2001; Winn et al. 2002). The quasi-stellar object, a blazar with a powerful jet, has redshift $z = 2.507$ (Lidman et al. 1999).

The lens distorts the extended radio emission from the jet and produces an semi-ring-like structure, along with two bright images separated by roughly one arcsecond (Jauncey et al. 1991). The Australia Telescope Compact Array observation at 8.6 GHz revealed these compact components, interpreted as emission from the jet core.

The radio monitoring program lasted for 18 months and resulted in the measurement of a time delay of $26^{+4}_{-5}$ days, and a magnification ratio of $1.52\pm0.05$ (Lovell et al. 1998). An independent measurement of the time delay using molecular absorption lines yields a delay of $24^{+5}_{-4}$ days, consistent with the result of radio monitoring (Wiklind & Combes 2001).
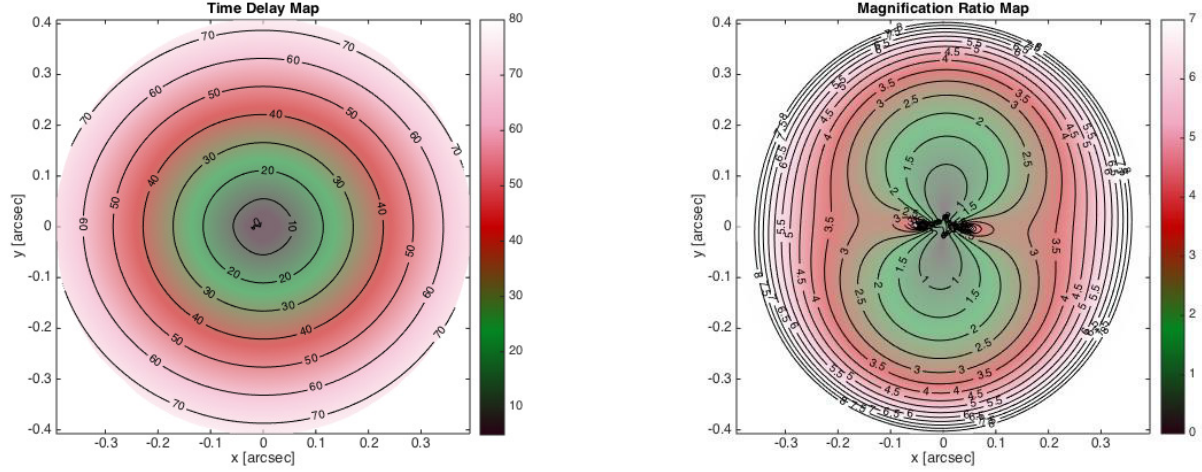
FIG. 1.— Maps based on the lens model of the lensing galaxy for PKS 1830-211 (Section 2.1). Left: Time delays between mirage images for different positions of the emitting region within the Einstein radius. Right: Magnification ratio map for different positions of the emitting regions in the source plane.

The images of PKS 1830-211 have prominent radio core-knot structures where the axis is roughly perpendicular to the line of separation of the two mirage images of the core. These radio observations define the projection of the jet. The mirage images of the core are separated by about 0.98 arcsec and aligned northeast (NE) and southwest (SW) in the plane of the sky (Nair et al. 2005; Garrett et al. 1997; Jones et al. 1996; Guirado et al. 1999). Jin et al. (2003) reported time dependent positional variations in the radio centroids at 43 GHz. Martí-Vidal et al. (2013) investigated the chromatic variability in resolved lensed images of PKS 1830-211 with ALMA to probe the jet base of this object.

Winn et al. (2002) modeled the lens parameters. Sridhar (2013) refined model and obtained a best fit for a singular isothermal ellipsoid (SIE) with ellipticity $e = 0.091$ and a lens oriented at $86.1°$ (for detailed definition of lens model see Keeton 2001a). We use these SIE lens parameters, the redshifts of the source and lens, and the Einstein radius of 0.491 arcseconds, to build time delay and magnification ratio maps. We base our maps on the *gravlens* code (Keeton 2001a,b).

Figure 1 (left) shows the time delays between mirage images of the emitting region in the source plane. For PKS 1830-211, the maximum time delay between the mirage images is $\sim 70$ days. In the outer region of the source plane, the magnification ratio between the mirage images can be $\gtrsim 10$. One of the images can thus be so faint that large time delays are undetectable. The right panel of Figure 1 shows a map of magnification ratios between mirage images of the emitting region located as a function of the position in the source plane.

To determine the position of emitting regions along the jet, we need to identify the position of the core and the alignment of the jet. Sridhar (2013) determine the position of the core based on the time delay (Barnacka et al. 2011) and magnification ratio reported by Martí-Vidal et al. (2013) along with the Hubble constant (Hinshaw et al. 2013). The red circle in Figure 2 delimits the region where the core is located.

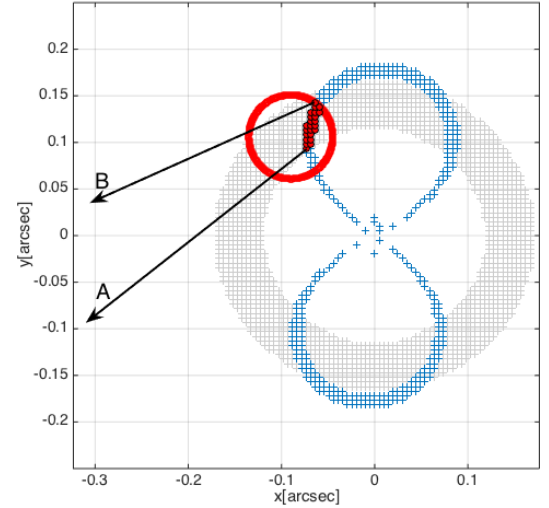Figure 3 shows the predicted total magnification, and



FIG. 2.— The range of possible core locations and the jet projections in the source plane. The gray area shows the allowed range ($1\sigma$ boundary) of the core positions with time delays from 21 to 30 days (Lovell et al. 1998). The corresponding magnification ratio between the resolved images is $1.52 \pm 0.05$. The blue area represents the positions of the core constrained by the magnification ratio measurement. The red circle delimits the allowed core positions derived by (Sridhar 2013). Arrows A and B indicate the limiting jet projections constrained by resolved radio images.

the time delay, and magnification ratios as a function of position along the jet. Once the time delays and magnification ratios are constrained by the light curve, we can use Figure 3 to identify the positions of the emitting regions.

## 2.2. *PKS 1830-211 as a Gamma-ray Emitter*

### 2.2.1. *Fermi/LAT Data Analysis*

PKS 1830-211 is a bright, high-energy emitter, detected for the first time at gamma rays by EGRET (Mattox et al. 1997). The *Fermi*/LAT satellite, a pair-conversion gamma-ray detector sensitive to photons in
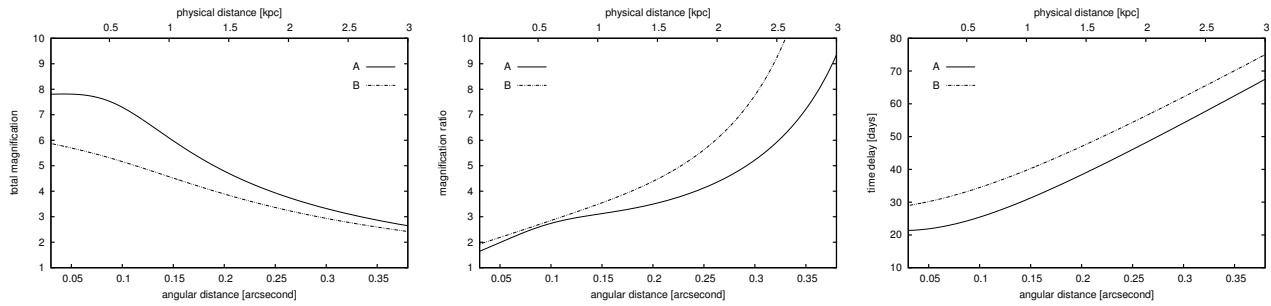
FIG. 3.— Time delays and magnification ratios as a function of the distance between the emitting region and the core. **Left**: Total magnification defined as the sum of the image magnifications. **Middle**: Magnification ratios along the limiting jet projections (indicated by arrows in Figure 2) **Right**: Time delays for emitting region located along the limiting jet projections.
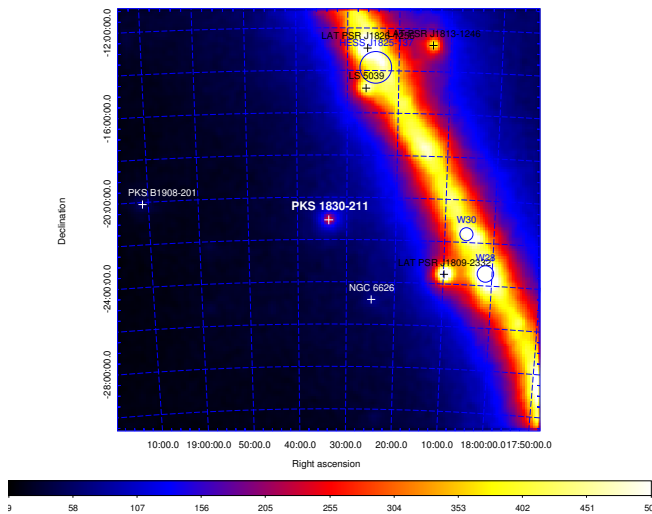


FIG. 4.— *Fermi*/LAT count map around PKS 1830-211. The map contains photons in the energy range from 200 MeV to 300 GeV.

the energy range from 20 MeV to 500 GeV (Atwood et al. 2009), also detects this source as a very bright gamma-ray emitter (Nolan et al. 2012). Our analysis of the *Fermi*/LAT data in the period from 54682 MJD to 57044 MJD, and in the energy range from 200 MeV and 300 GeV, shows detection of the source at a level of 94 $\sigma$. We analyze the *Fermi*/LAT Pass7 events and spacecraft data using standard likelihood tools distributed with the Science Tools v9r32p5 package available at the *Fermi* Science Support Center webpage.

For source detection and for detection of the time delay, we only used events with the highest probability of being photons, those in the CLEAN class. We exclude events with zenith angles $> 100°$ from the analysis to limit contamination by Earth albedo gamma rays. In addition, we remove events with a rocking angle of $> 52°$ to eliminate time intervals when the Earth entered the LAT Field of View (FoV).

PKS 1830-211 is about $\sim 5°$ from the galactic plane (Galactic coordinates, $l = 12.°2$, $b = -5.°7$). Thus, to avoid large background contamination, we analyze only events with reconstructed energies above 200 MeV and selected within a square region of $10°$ radius centered on the coordinates of PKS 1830-211 ($ra = 278.41333$, $dec = -21.07492$). Figure 4 shows the *Fermi*/LAT count

map around PKS 1830-211. The source is clearly well-separated from the Galactic plane and there are no significant nearby sources.

To build the gamma-ray light curves, we use a binned-maximum likelihood method (Mattox et al. 1996); we model the background using a galactic diffuse emission model (gll_iem_v05), and an isotropic component (iso_clean_v05) available at the *Fermi* Science Support Center webpage. The fluxes are derived from the post-launch instrument response functions P7REP_CLEAN_V15.

The XML source model input to the binned maximum analysis contains all the sources included in the Second *Fermi*/LAT catalogue (Nolan et al. 2012) within an annulus of $20°$ around the region of interest (ROI). We first analyze the data based on the XML source model with free parameters for the sources within $7°$; the parameters at larger radius are fixed to their 2FGL values. We use this XML source model to produce the light curves.

### 2.2.2. *Gamma-Ray Light Curves*

We begin by producing the light curve starting from the launch of the *Fermi*/LAT satellite in August 2008 through February 2015. Figure 5 shows the light curve for this period with 7 day binning. The energy spectrum of the entire period is well described by a power law with $\Gamma = 2.54 \pm 0.01$ and an integral flux of $F(0.2 - 300\,\mathrm{GeV}) = (1.94 \pm 0.02) \times 10^{-7}\,\mathrm{ph\,cm^{-2}s^{-1}}$. The highest energy event recorded by the *Fermi*/LAT was 50 GeV, detected in the time window 55389 MJD - 55395 MJD. Thus detection of PKS 1830-211 may be possible with H.E.S.S. II.

Figure 5 shows several active periods. We define active periods as times when the gamma-ray emission exceeds the average flux by least $2\sigma$. This approach yields four active periods. The first series of very bright flares detected by the *Fermi*/LAT satellite occurs in the period 55420 MJD to 55620 MJD. The second series of flares occurs in the period 56050 MJD to 56200 MJD. Next, a bright single flare occurs around July 28, 2014. Recently, on January 8, 2015, another flare occurred. Figure 6 shows the light curves of these bright flares.

### 3. TIME DELAY MEASUREMENT

Gravitationally-induced time delays are fundamental measurements in cosmology because, in principle, they provide a measurement of the Hubble constant independent of the distance ladder (Refsdal 1964; Schechter et al. 1997; Treu & Koopmans 2002; Kochanek 2002; Koopmans et al. 2003; Oguri 2007; Suyu et al. 2013; Sereno &
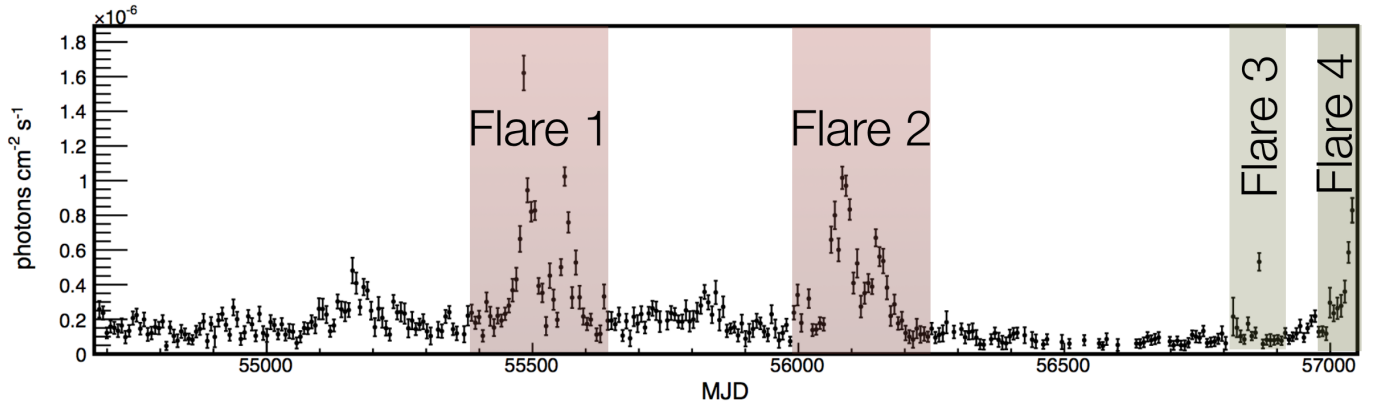
FIG. 5.— *Fermi*/LAT light curve of PKS 1830-211 from August 2008 through February 2015. The fluxes are based on seven-day binning. The energy range is 200 MeV to 300 GeV.

Paraficz 2014).

Monitoring of gravitationally lensed sources at both radio and optical wavelength where the mirage images are resolved provide a basis for a number of measured time delays (Fassnacht et al. 2002; Eulaers & Magain 2011; Rathna Kumar et al. 2013; Tewes et al. 2013; Eulaers et al. 2013). Unevenly spaced data resulting from, for example, weather and/or observing time allocation, are a challenge for light-curve analysis. A number of techniques have been specially developed to utilize these multiple light curves of mirage images with unevenly sampled data (Edelson & Krolik 1988; Press et al. 1992; Rybicki & Press 1992; Burud et al. 2001; Pelt et al. 1998; Pindor 2005; Scargle 1982; Roberts et al. 1987; Geiger & Schneider 1996; Gürkan et al. 2014; Hirv et al. 2011).

Gamma-ray observations have very low spatial resolution but long, nearly uniform time coverage. In particular, the *Fermi*/LAT detector provides a very long, evenly sampled, light curve, of almost 7 year duration. Furthermore, the photon noise is low. At gamma-ray energies, the mirage images cannot be resolved. The observed light curve is thus a sum of the images. The mirage images have similar time evolution, but they appear shifted in time and with different magnification. For any particular position of the emitting region the time delay and corresponding magnification ratio are fixed. Here the challenge is to extract the time delay and magnification ratio from the time series informed by the model results based on shorter wavelength data (Figure 3).

In the following sections, we investigate three different methods of determining time delays from unresolved light curves: the standard Autocorrelation Function (Section 3.2.1), the Double Power Spectrum method (Section 3.2.2), and the Maximum Peak Method (Section 3.2.3). Using Monte Carlo simulations, we evaluate the significance levels for these methods, and their sensitivity in detecting the gravitationally-induced time delays. The Appendices show the detailed steps for the Double Power Spectrum (Appendix A.2.1) and for the Maximum Peak Method (Appendix B). We use PKS 1830-211 as a prototype for broader application of these techniques.

## 3.1. *Settings for the Monte Carlo Simulations*

Monte Carlo simulations are a traditional and powerful tool for calibrating the analysis of time series. They are important in the case of sparsely sampled data and they are necessary for evaluating the significance of an apparent time delay detection (Vaughan 2005).

In this section, we describe the settings for our Monte Carlo simulations. We include the characteristics of the time series, the procedures for evaluating the significance of time delay detections, and the sensitivity of the methods for detecting gravitationally-induced time delays in unresolved light curves. The full analysis takes advantage of the physical relationship between the time delay and the magnification ratio.

### 3.1.1. *Characteristics of the Signal*

The observed temporal behavior in blazars is represented by power law noise (Finke & Becker 2014; Hayashida et al. 2012; Nakagawa & Mori 2013; Sobolewska et al. 2014) where the power spectral density (PSD) is inversely proportional to the frequency, $f$, of the signal to the power $\alpha$:

$$S(f) \propto 1/f^\alpha. \qquad (1)$$

This random variability is often referred to as *noise* intrinsic to the source (not a result of the measurement error), which is a result of stochastic processes (Vaughan et al. 2003). Astronomers refer to these stochastic fluctuations as *signal*; in other fields, the most common terminology is *noise* (Press 1978). For ease of presentation, we adopt this more general terminology and explore properties of various types of noise.

Typically, quasars have $\alpha \sim 1 - 2$ (Equation 1). The average slopes for gamma radiation from the brightest 22 flat spectrum radio quasars and from the 6 brightest BL Lacs are 1.5 and 1.7, respectively (Abdo et al. 2010). During the gamma-ray quiescent state, where blazars remain most of the time, the fluctuations in the flux are small, and the temporal behavior is characterized by power law noise with index $\sim 1$. During flaring, the amplitude of the fluctuation of the flux can increase by a few to dozens. The signal is still represented by the power law noise, but with a greater index $\alpha$.

In our simulations, we produce artificial light curves with time series represented by red and pink noise. Red noise, also known as a Brown noise, has $\alpha = 2$, consistent with the observed behavior of many gamma-ray active periods. Figures 6 shows flaring periods of PKS 1830-211, and Figure A1 shows an example of an artificial light
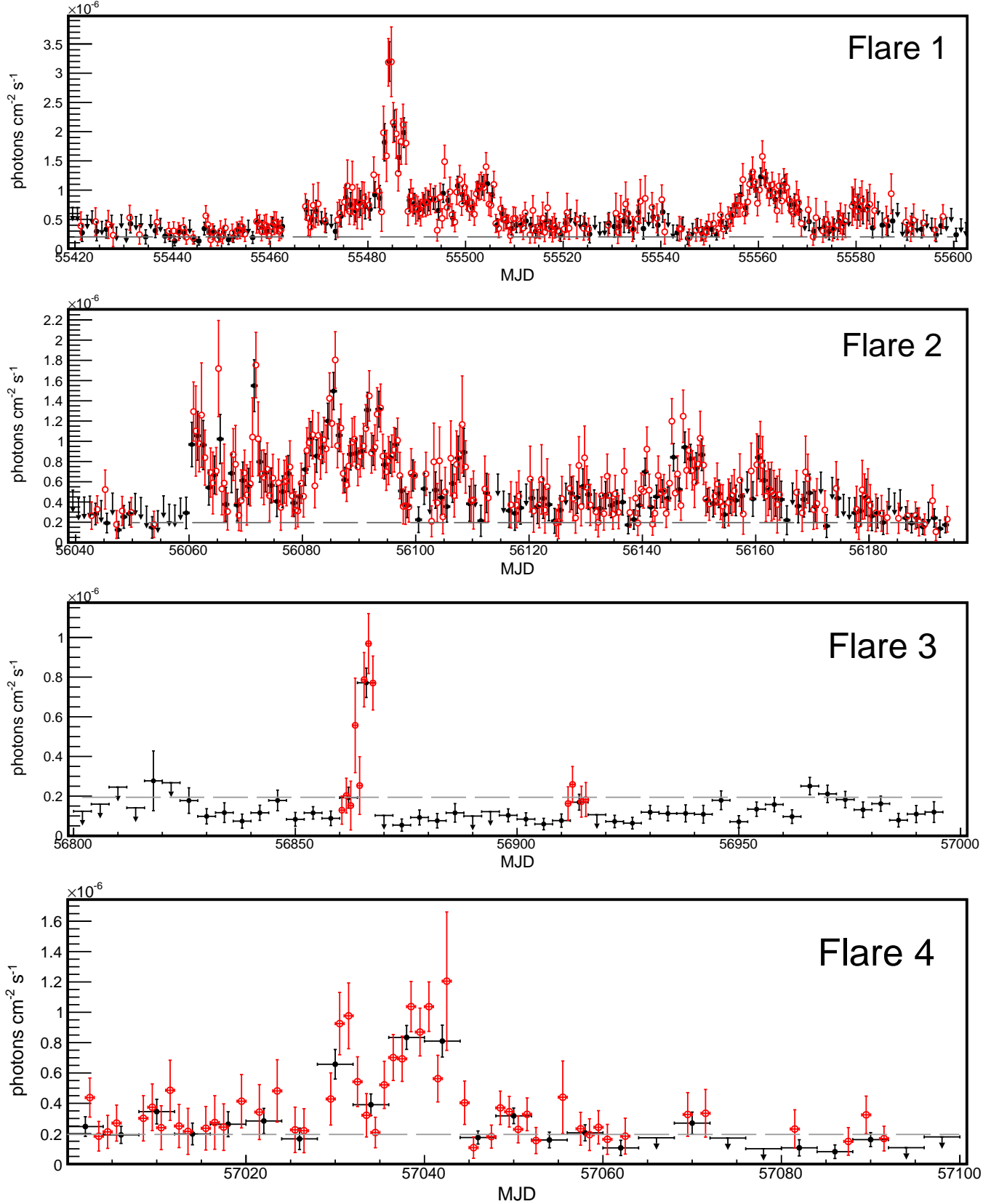
Barnacka et al.



FIG. 6.— *Fermi*/LAT light curves of flaring PKS 1830-211. We show Flare 1 and Flare 2 with one-day binning (black-filled circles), and with 12-hour binning (red open circles). We show Flare 3 and Flare 4 with four-day binning (black-filled circles), and one-day binning (red open circles). We show red points only for bins with at least $2\sigma$ detection. The green dashed line represents the average flux $(1.94 \pm 0.02 \times 10^{-7}\,\mathrm{photons\,cm^{-2}\,s^{-1}})$ measured from the 7 years light curve of PKS 1830-211 in the energy range from 200 MeV to 300 GeV.

curve based on red noise, with and without an artificially induced gravitational time delay. The time structure of the observed and simulated light curves is remarkably similar by eye.

Pink noise has a power spectrum inversely proportional to the frequency of the signal ($\alpha = 1$); this type of noise describes the temporal behavior in the gamma-ray quiescent state. For demonstration purposes, we also construct artificial light curves of white noise, $\alpha \sim 0$. We use these types of noise to demonstrate the sensitivity of time delay detection to the nature of the underlying signal along with the method of analysis.

We conducted our simulations and analysis using the Matlab environment. We generated samples of power law noise using the Little et al. (2007) code.

In general, the temporal behavior of blazars is simply represented by power law noise. The lensed light curve is still power law noise, but it contains information about the time delay. The lens itself is not a gamma-ray emitter at a detectable level. Therefore, we can construct the observed gamma-ray light curve as a sum of the lensed components of the blazar:

$$S(t) = s(t) + s(t+a)/b, \qquad (2)$$

where $S(t)$ is the unresolved light curve of the lensed blazar, composed of the sum of the mirage images. The temporal behavior of individual images is determined by the source, but the images are shifted in time by the gravitationally-induced time delay, $a$, and with the magnification ratio between mirage images, $b$.

Data from the *Fermi*/LAT satellite allows construction of an 7 year-long light curve (see Figure 5). We focus on the nature of the gamma-ray emission during flaring activity. The durations of these active periods range from a few to hundreds of days (see Figure 6).

The lens model predicts time delays up to $\sim 70$ days. To have a chance of investigating the entire permitted range of time delays, the sample has to be at least twice as long as the maximum time delay. In our simulations, we produced time series of 155 days, exactly the duration of the active period of Flare 1.

The *Fermi*/LAT detector continuously monitors the entire sky, but, sometimes, the photon flux of the source can be too low to be detected significantly in a time bin chosen *a priori*. There is no gap in the time series, but the flux from the source cannot be detected at $\gtrsim 2\sigma$. In these cases, we compute an upper limit on the flux. The value of upper limits does depend, for example, on the exposure within the time bin. Thus, if we use upper limits as a measure of a flux, satellite-related periodicities can appear in the signal. Another approach is to set the flux to zero in these low photon flux bins. We check the impact of both approaches (Section 4.1).

One can also interpolate the flux or set the flux to an average value. However, this approach could introduce a flux, in a particular, that exceeds the observed upper limit, thus invalidating the time series analysis. We thus do not investigate this approach.

Monte Carlo simulations can also provide a strong test of the method for treating data points with upper limits. We can readily introduce the estimated upper limits into simulated time series and treat the detections and upper limits in an internally consistent way. This approach gives us a measure of the impact of bins with upper limits

only on the significance of the detection. We discuss this issue further in the results section, where we describe the temporal analysis of the PKS 1830-211 light curves.

### 3.1.2. *Statistical Significance*

A crucial element of the analysis is evaluation of the statistical significance of the detection of a time delay. An observed modulation of the signal could be a real time delay or it could arise purely by chance. Monte Carlo simulations provides a way to compute the probability of detections as opposed to false positives (see e.g. Vaughan 2005).

We produce $N = 10^6$ artificial light curves of power law noise characterized by $\alpha = \{0, 1, 2\}$. We calculate the chance that a particular time delay signal will appear randomly in the simulated light curve which contains no intrinsic time delays. For each simulated light curve, the output consists of time delays and the relative power of the signal as a function of the time delay. We construct the cumulative probability distribution of false detection (CPD: p(POWER)) for each time delay as a function of the power. The cumulative probability of a false detection is less than $p$. We investigate $p = 0.317$ $(1\,\sigma)$, $p = 0.0455\,(2\,\sigma)$, $p = 0.0027\,(3\,\sigma)$, and $p = 0.00006$ $(4\,\sigma)$, respectively, for each analysis method and for each of the three representative noise spectra. We show the results in Sections 3.2.1 and 3.2.2. The CPDs are sensitive both to the underlying noise spectrum and to the analysis method.

### 3.1.3. *Detectability of the Time Delay*

We also use the Monte Carlo simulations to assess the chance of detecting a real signal at a given significance level. Here the simulated light curves we construct for the analysis contain artificial time delays with the appropriate magnification ratio. For each combination of noise spectrum, time delay and magnification ratio, the detectability depends on the analysis method. In some cases where, for example, the magnification range is large and the time series is too short, some methods can not detect the time delay at all.

The lens model predicts a range of time delays and corresponding magnification ratios. For each time delay in the range from 1 to 80 days along with the corresponding magnification ratios, we produce $10^5$ artificial light curves of power law noise with artificially induced time delays. We distribute the time delays uniformly on the interval 1 to 80 days with a 1 day interval (the same as the light curve binning). These light curves simulate the observations of PKS 1830-211.

The observed light curve is a sum of components. The first component (the first mirage image), $s(t)$, is just power law noise. The second component is the same noise, but shifted by the time delay, $a$, and with magnification ratio, $b$. Thus, the second component is $s(t+a)/b$. The final observed light curve is the sum of these components. We simulate analogous artificial light curves with red noise ($\alpha = 2$) to evaluate the probability of time delay detection in the observed flaring light curve. To assess time delay detectability in quiescent light curves we analyze simulated light curves based on pink noise ($\alpha = 1$). For demonstration purposes, we also check the detectability of a time delay for white noise light curves ($\alpha = 0$).

Analysis of the artificial light curves gives the probability of detecting the time delay at $1\,\sigma$, $2\,\sigma$, $3\,\sigma$, and $4\,\sigma$ levels. From the simulations with no inherent time delays, we know the power where the detection rate of false positives is at a given significance level. At each power (corresponding to a particular significance level), we can then check how many simulated light curves have power above this limit. We do this analysis for each time delay and significance level for false positive detection.

We discuss the results of this analysis in Sections 3.2.1 and 3.2.2. As in the case of the analysis of false positives, the results for detection of a true time delay depend on the input spectrum, the analysis method, and the combination of time delay and magnification ratio.

### 3.2. Methods

#### 3.2.1. Autocorrelation Function

The Autocorrelation Function (ACF) is a standard tool for estimating time lags in light curves. The ACF of a signal describes the correlation of the values of the samples at one time on the values at another.

We investigate the probability of detecting spurious time delays that arise from fluctuations in power law noise. We evaluate the detectability of simulated time delays.

We represented the time series as drawn from power law noise with $\alpha$. For larger $\alpha$, the time series contains more apparent structure; there are more and larger amplitude variations on shorter time scales. Thus a time delay detection is, in principle, easier for a source characterized by larger $\alpha$. However, the steep spectrum of power law noise can also more easily produce spurious peaks in the ACF, thus raising the confidence levels artificially.

Figures 7 and 8, show results of the Autocorrelation Function applied to Monte Carlo simulations of $10^5$ time series for white, pink, and red noise. As indicated, white noise does not cause spurious time delays with large power: the confidence boundaries are low ($\sim 0.3$ for $1\,\sigma$), and flat over the full range of time delays we explore. However, the probability of detecting time delays in the signal characterized by white noise using the ACF is very low. The probability of detecting a signal at the $1\,\sigma$ level does not exceed 35%, or 5% at the $2\,\sigma$ confidence level.

Red and pink noise have a larger potential for producing spurious peaks in the ACF, (figure 7); in these cases, the confidence boundaries are elevated. For simulated time series, the ACF is most sensitive for time delays in the range $\sim 5$ days to $\sim 40$ days. The detection of long time delays is limited by the finite length of the sample; the simulated length corresponds to 155 days. Furthermore, mirage images separated by longer time delays also have larger magnification ratio resulting in an attenuation effect that hinders the detection.

#### 3.2.2. Double Power Spectrum

The Double Power Spectrum (DPS) was the basis for detection of the first gravitationally-induced time delay at gamma-rays (Barnacka et al. 2011). Here we review the method and we show the individual step in Appendix A. The steps in this signal processing are based on widely used methods (Oppenheim & Schafer 1975; Brault & White 1971), and have been described in Barnacka et al. (2011); Barnacka (2013).

The signal in the time domain is equation (2). The Fourier transform of the first component, $s(t)$, is $\tilde{s}(f)$, and the second component transforms to the frequency domain as $\tilde{s}(f)e^{-2\pi i f a}$. Therefore, the observed signal $S(t)$ transforms into

$$\tilde{S}(f) = \tilde{s}(f)(1 + b^{-1}e^{-2\pi i f a}), \qquad (3)$$

in Fourier space.

The first power spectrum of the source is the square modulus of $\tilde{S}(f)$:

$$|\tilde{S}(f)|^2 = |\tilde{s}(f)|^2(1 + b^{-2} + 2b^{-1}cos(2\pi fa)). \quad (4)$$

The first power spectrum is the product of the "true" power spectrum of the source, $|\tilde{s}(f)|^2$, times a periodic component with a period (in the frequency domain) equal to the inverse of the relative time delay $a$. Thus, to find time delay $a$, we need to find the period of the pattern in the first power spectrum. The transformation of the first power spectrum, which is in the frequency domain, to Fourier space, brings us back to the time domain, where the amplitude of the signal corresponds to the power of the time delay signal present in the original time series. The method is similar, in spirit, to the Cepstrum method widely used in speech processing and seismology (Bogert et al. 1963).

We use a Monte Carlo procedure to evaluate the performance of the DPS for power law noise. Figure 9 shows the confidence levels of $1\,\sigma$, $2\,\sigma$, $3\,\sigma$, and $4\,\sigma$, for white, pink and red noise, respectively.

The Monte Carlo simulation demonstrates the effectiveness of the signal processing. The Double Power Spectrum method emphatically enhances the probability of significant detection of time delays. The probability of detecting a time delay in the range from 5 to 40 days, at $3\,\sigma$ level is in the range from 90% to 40% in contrast with the ACF method where the probability is 10% at best. The signal processing in DPS eliminates the large dependence of significance levels and the probability of detection of time delay, on the index $\alpha$ of power law noise.

The efficiency of detecting longer time delays is limited only by the sample length and the magnification ratio between the mirage images. We follow the same procedure independent of the time delay. In principle, one can optimize the signal processing procedure for different ranges of time delays to account for the effects of signal attenuation and discontinuity at the begin and end of time series.

#### 3.2.3. Maximum Peak Method

The temporal behavior of the active period of gamma-ray radiation from jets is characterized by distinctive flares where the emission can rise by a factor of a few to dozens relative to the average gamma-ray flux from the source. The duration of a single flare is usually short, from a few hours to a few days. Thus, the duration of the flares is much shorter than the typical time delay. The short duration of the flares relative to the expected time delays are an important element in analysis of unresolved light curves. Because gamma-ray flares can be identified as distinct events in the time series, and we know the range of expected time delays and corresponding magnification ratios, we can search for echo flares in successive bins directly.
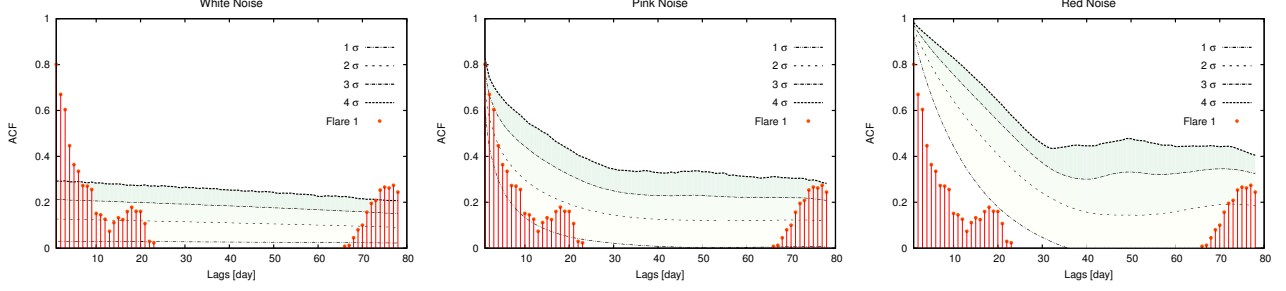
FIG. 7.— Confidence level for the autocorrelation method derived from Monte Carlo simulations of $10^5$ light curves for white (left), pink (middle), and red (right) noise. Autocorrelation coefficients as a function of the time delay. The lines indicate $1\sigma$, $2\sigma$, $3\sigma$, and $4\sigma$ confidence levels. The red points show the ACF for Flare 1.
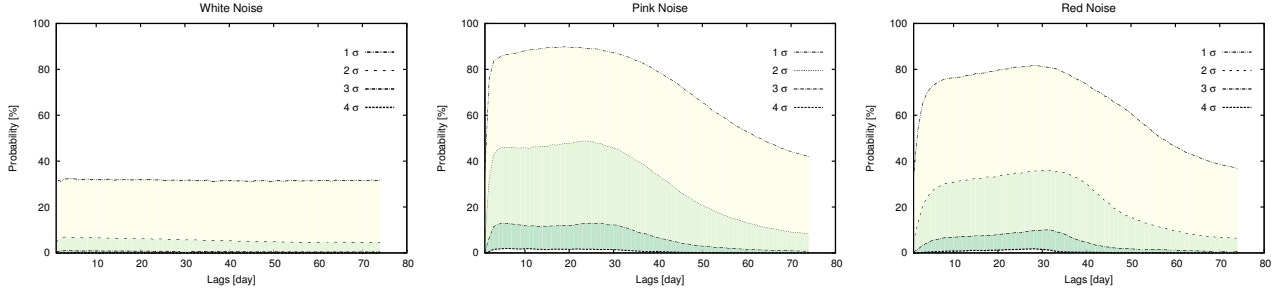


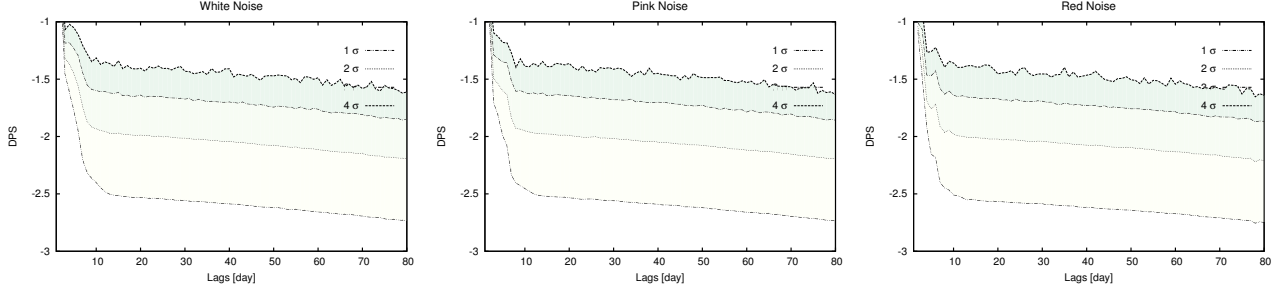FIG. 8.— Probability of detecting a time delay at a given significance level with the Autocorrelation method.



FIG. 9.— Confidence levels for the Double Power Spectrum method.
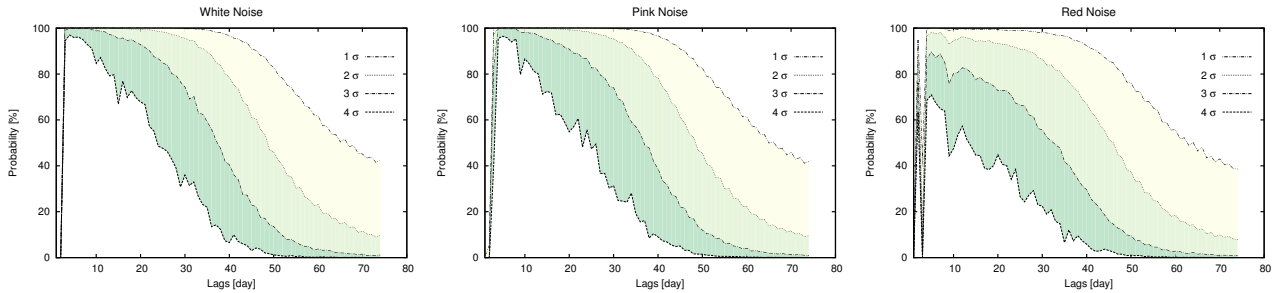


FIG. 10.— Probability of detecting a time delay at a given significance level based on the DPS method.

The gamma-ray active state can last for a dozen to even hundreds of days; these periods consist of a series of individually identifiable flare. Methods like the ACF or the DPS are well suited for analyzing these longer periods of activity when light curve can be extracted with shorter binning ranging from 12 hours to 1 day. When the active period consists of a single short flare, bins with a longer integration time are necessary. The gamma-ray flux before and after these single flares corresponds to the quiescent state. Thus to detect the signal at a significant level we must increase the size of the bin (exposure).

The MPM method complements the DPS method particularly for these isolated flares. In this method, we identify the first brightest flare, and calculate the flux ratio between the bin with the largest flux (the flare) and flux in successive bins. These flux ratios constrain the magnification ratios which are not constrained by the DPS method.

The MPM method enables us to extract additional physical constraints from the time series. We compare calculated ratios, as a function of a time delay between a particular bin and the position of the brightest flare, to the magnification ratios as a function of the time delay predicted from the model. We identify the time delays where the ratio of fluxes is consistent with the predicted magnification ratio. These bins might or might not exist. If there are bins consistent with the expected delays, the data support the picture based on the model. It is important to note here that the model takes constraints from data at other wavelengths into account. This method of analysis of the light curve especially allows us to exclude ranges of time delays where there is no consistent magnification ratio observed ($\sim 80\%$ of the range).

We demonstrate the method with Monte Carlo simulations in Appendix B. We investigate this approach for cases with a single flare and with a series of flares.

### 4. RESULTS

Here, we apply the techniques of Section 3 to the flaring gamma-ray light curve of PKS 1830-211. We use PKS 1830-211 as an example of the way that these analysis methods can elucidate the origin of the gamma ray flares. In particular, we demonstrate that the flares probably do not all originate from the same location in the source.

In the light curve (Figure 5) there are two long active periods (red area; Flares 1 and 2) of more than 100 days and two isolated individual flares (green area; Flares 3 and 4). We analyze each of these four flaring periods separately.

#### 4.1. Gamma-Ray Flare 1

Figure 6 shows Flare 1 with 1-day and 12-hour binning. The length of the light curve is 155 days. The temporal behavior is characterized by a set of very bright flares. Between the flares the flux is close to the long-period average (covering the entire light curve); there are upper limit detections for $\sim 60$ days in total. The fit to the power spectral density results in $\alpha = 1.45$, between pink and red noise. Figure 11 shows the Autocorrelation Function of Flare 1.

We investigate two approaches to the upper limits. In one approach, we use the measured value of an upper limit as the flux. In the second approach, we set the flux to 0 in time bins with upper limits only. The ACF
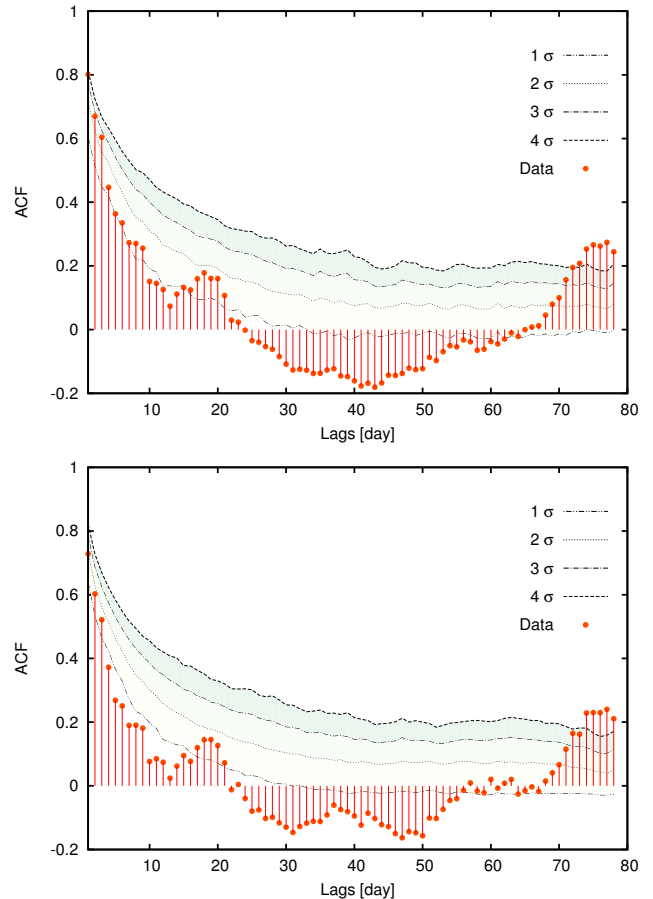


FIG. 11.— Autocorrelation function for **Flare 1** along with confidence levels.
**Top**: Autocorrelation function for Flare 1 based on upper limits as measures of the flux. The confidence levels are based on MC simulations of power law noise, with upper limits as measured for Flare 1.
**Bottom**: Autocorrelation function for the light curve of Flare 1 with the flux set to 0 in time bins with upper limits. The confidence levels are derived by generating time series of power law noise, with values set to zero in bins that have measured upper limits.

does not show a significant difference in time delays and confidence level estimates for these two ways of treating the upper limits.

The intrinsic variability of the source is consistent with the $1\,\sigma$ confidence level. The ACF shows a broad feature at a time delay of $17.9 \pm 7.1$ days at $\sim 2\,\sigma$ level. This result agrees with time delay estimated with the ACF performed by Abdo et al. (2015), $19 \pm 1$ days.

The other broad feature appears at $76 \pm 20$ days and exceeds the $4\,\sigma$ level. However, given the model of the lens, this value reaches the maximum allowed time delay. At time delay of $\sim 70$ days, the magnification ratio between the mirage images is larger than 10, and, as we have demonstrated with Monte Carlo simulations (Figure 8), the probability of detecting such gravitationally-induced time delays at the $4\,\sigma$ level using the ACF is close to zero. Thus, this feature is probably not produced by a gravitationally-induced time delay, but rather reflects the time difference between subsets of flares around 55485 MJD and 55560 MJD.

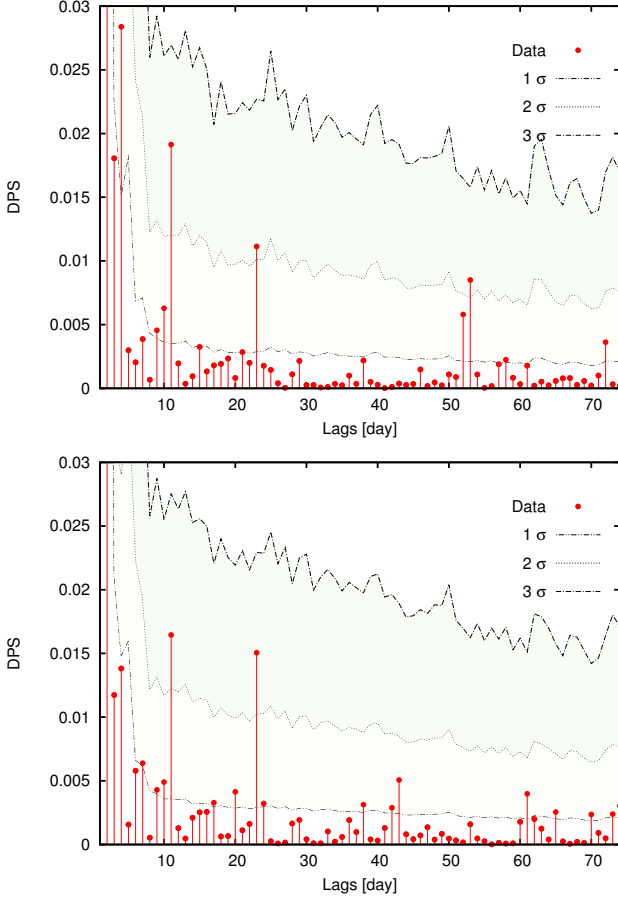Figure 12 shows the analysis of the same time period

FIG. 12.— Double Power Spectrum for **Flare 1** in arbitrary units with confidence levels.
**Top**: DPS based on upper limits as a measure of the flux. Confidence level are based on MC simulations of power law noise, including the upper limits as measured for Flare 1.
**Bottom**: DPS with the flux set to zero for time bins with upper limits. Confidence levels are based on MC simulations also with zeros corresponding to upper limits.
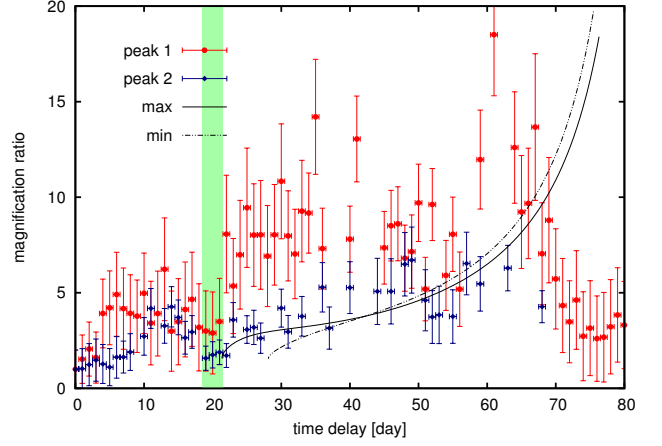


FIG. 13.— The Maximum Peak Method applied to **Flare 1**. Red points correspond to successive outbursts detected on 55484 MJD. Blue points represent the ratio between the outburst at 55560 MJD and successive bins. To estimate the errors in the magnification ratio we use the flux error at the maxima. The area between the solid and dashed lines represents the allowed range of magnification ratios in the parameter space defined by the possible projections of the jet in the lens plane (Figure 2). The green area represents the range of time delays where the observed magnification ratio is consistent with the model predictions.

but with the Double Power Spectrum, and illustrate the result of different approaches to the upper limits. The DPS method is much more sensitive to signal detection resulting in sharp peaks around the time delays. Introducing the values of upper limits as a measure of the flux results in a peak at a time delay of $\sim 52 \pm 1.5$ day. This time variation corresponds to the precession period of the *Fermi* spacecraft of 53.4 days[1]. This result demonstrates the sensitivity of the DPS in detecting even a faint signal in the time series.

The DPS method detects two time delays at $11 \pm 0.5$ days and $23 \pm 0.5$ days above the $2\sigma$ level. The significance of the detection is consistent with expectations for these time delays (see Figure 10).

To further investigate whether the time delays that appear in the DPS method are induced by the gravitational lensing of a flaring emission region, we use the Maximum Peak Method which combines the observations with the predictions of the lens model. Figure 13 shows magnification ratios between the two successive periods following the two largest outburst in the Flare 1. To conclude that

the detected time delay is indeed induced by the gravitational potential of the lens, we require that both subsets of flares have magnification ratios consistent with the time delay. The time delay of $11 \pm 0.5$ days is inconsistent with the model. This time delay may be a harmonic of the 23-day delay or it may be a previously undetected instrumental effect. Figure B3 shows an analysis of a randomly selected simulated light curve where a harmonic appears at this delay.

The time delay of $\sim 23$ days is consistent with the magnification ratio for both subsets of flares. Thus, this time delay of $23 \pm 0.5$ days is probably gravitationally induced, and constrains the spatial origin of the Flare 1.

### 4.2. *Gamma-Ray Flare 2*

The second set of flares appeared in the time period 56043 MJD to 56194 MJD. Figure 6 shows the light curve for this time period. The power spectral density is represented by a power law with an index $\alpha = 1.3$. We use this index in Monte Carlo simulations to evaluate the confidence levels for signal detection.

The ACF (Figure 7) shows two features at a significance level close to 2; the first occurs at a time delay of $10.1 \pm 2.5$ days, and the second at $21.1 \pm 2.7$ days.

The DPS method shows detection of the same features (see Figure 9). The first feature appears as a double peak at 11 and 13 days at a significance level greater that $2\sigma$. As in the case of Flare 1, the 11-13 day delay is inconsistent with the lens model and may be a harmonic or instrumental effect. The other peak at $19.7 \pm 1.2$ days is detected at a significance level greater then $3\sigma$.

For Flare 2, The Maximum Peak Method, (see Figure 14), shows a magnification ratio consistent with the model predictions for time delays in the range from 20 to 23 days. Thus, the time delay of $19.7 \pm 1.2$ days is consistent with the time delay expected for the position of the core, and is probably a result of gravitational lensing of the flaring gamma-ray region.
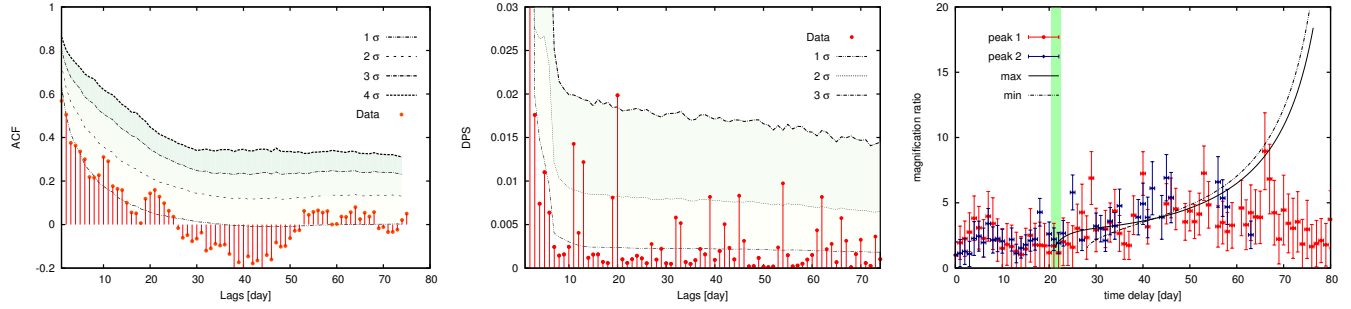
FIG. 14.— Time delay estimation for **Flare 2**. **Left:** Autocorrelation Function with confidence levels. **Middle:** Double Power Spectrum method with confidence levels. **Right:** Maximum Peak Method, peak 1 corresponds to the flare at 56072 MJD, and peak 2 is a ratio calculated relative to the flare at 56146 MJD. Solid and dotted lines indicate predicted magnification ratios along the jet indicated as the arrows A and B in Figure 2.
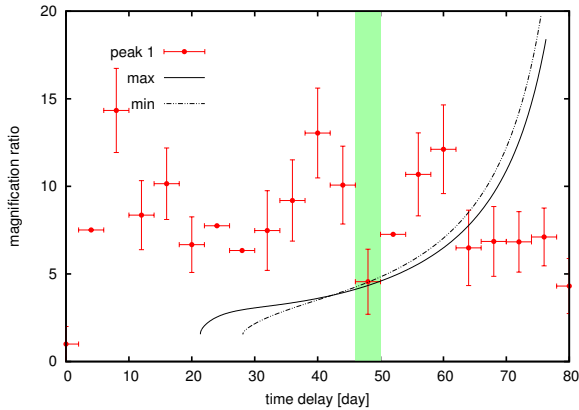


FIG. 15.— Maximum Peak Method applied to **Flare 3** on July 28.

### 4.3. *Gamma-Ray Flare 3*

The third flare occurred on July 28 and lasted for a few days. Figure 6 shows the gamma-ray light curve around that period. During the flare, the emission increased by a factor of 5 relative to the average flux. The flux for a period of at least 80 days before and after Flare 3 is at or below the average flux.

Figure 15 shows the results of the Maximum Peak Method. The time delay range consistent with the expected magnification ratio appears at 46 - 50 days, and corresponds to an increase in the flux recorded at 56912 MJD. To further investigate whether this period of activity is indeed an echo of the flare which occurred at 56865 MJD, we construct a light curve around that period with a time binning of 1 day.

The delayed counterparts should have similar time evolution. The red points in Figure 15 show that these two episodes do not have identical time evolution. The bin around 56865 MJD consists of flux close to the average for the source; thus the bin may contain significant contribution from the photons originating from the quiescent state.

In any case, Flare 3 must have a time delay equal or larger than 48 days. The secure detection of such a long time delay is beyond the sensitivity of the ACF and the DPS for such a short light curve with time bins of 4 days.

If Flare 3 originated from the core, we would expect a time delay in the range 20 to 30 days. Even with the short light curve, we would expect to detect the echo flare; in the initial flare the flux increases by a factor of $\sim 5$ and the echo flare should appear with a flux at least twice the average. Absence of a detection in this range between 20 and 30 days makes it clear that Flare 3 does not originate from the core region. For a time delay $\gtrsim 50$ days, Flare 3 must originate at a projected distance from the core $\gtrsim 1.5$ kpc (see Figure 3).

### 4.4. *Gamma-Ray Flare 4*

The most recent gamma-ray activity of PKS 1830-211 (Figure 6) consists of two flares. For the temporal analysis, we use a light curve with one-day binning consisting of 90 days. The Autocorrelation Function, the Double Power Spectrum, and the Maximum Peak Method do not show time delays consistent with origination in the core (Figure 16). The DPS method indicates a time delay at 11.8±0.8 days with a significance of $\sim 2\sigma$; however this time delay is inconsistent with model based on radio observations and is thus probably a false positive. The time delay of $\sim 11$ days accidentally corresponds to the time between the two flares. The first flare was brighter than the average flux for about 4 days and peaked around 57032 MJD. The second one lasted for about 9 days and appeared 2 days after the first one. These flares have very different temporal evolution, thus, are not echoes of one another.

Again, the lack of detection of the time delay in the range between 20 and 30 days shows that Flare 4 does not originate from the core region. The analysis method is sensitive for time delays $\lesssim 50$ days and there are no other detections. The data show that the time delay must be greater than $\sim 50$ days and thus the radiation must originate from a region located at projected distance from the core $\gtrsim 1.5$ kpc (see Figure 3).

### 5. DISCUSSION

Lensing resolves the gamma-ray emission of PKS 1830-211 during its flaring periods and limits the origin both to the core and to regions displaced by $\gtrsim 1.5$ kpc along the jet. Flares 1 and 2 originate from a region of $\sim 100$ pc around the core. At the redshift of $z = 2.507$, where PKS 1830-211 is located, a projected distance of 100 pc corresponds to $\sim 0.02$ arcsecond. Thus, this lens improves the angular resolution at gamma-ray $\sim 10000$ times (Figure 17).

Resolving the high energy universe using cosmic lenses relies on the ability to measure time delays and to model the mass distribution of the lens. The localiza-
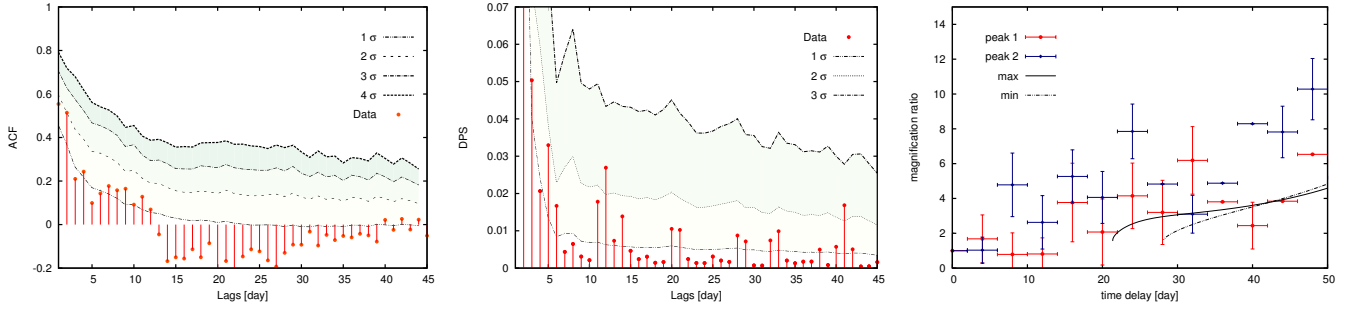
FIG. 16.— Time delay estimation for **Flare 4**. **Left:** Autocorrelation Function with confidence levels. **Middle:** Double Power Spectrum method with confidence levels. **Right:** Maximum Peak Method, peak 1 corresponds to the bin centered at 57030 MJD, and the peak 2 is a ratio calculated relative to the time bin centered at 57038 MJD. Solid and dotted lines indicate the predicted magnification ratios along the jet shown as the arrows A and B in Figure 2.

tion to 100 pc in this gravitationally-lensed system corresponds to an uncertainty in time delay measurement of 5 days. The Double Power Spectrum method is an effective approach for measuring the time delay (Section 3.2.2 and Appendix A). This method can extract time delays from gamma-ray light curves with an accuracy down to 0.5 days. In principle, this accuracy can provide a localization of the source to ∼ 10 pc.

A limiting factor in any lensing analysis is the precise model of the lens and alignment of the jet. We have used a very conservative position of the core and the jet alignment. In principle, more detailed analysis of all of well-resolved radio images can yield better constraints, but this analysis is beyond the scope of this paper.

For these complex sources, there are always puzzles. The lack of detection of time delays following Flare 3 and Flare 4 could indicate some other physical source for increased emission. The first possibility is microlensing. Flare 3 and Flare 4 are unlikely to be microlensing events because the typical time scale of a caustic crossing microlensing event is of the order of months to years (Wambsganss 2001); Flares 3 and 4 have a typical duration of days and a time structure characteristic of gamma-ray flares.

The size of the emitting region (the source size effect) might impact the magnification ratio for Flares 3 and 4. A spatially larger emitting region results in a larger magnification ratio (see Figure 2 in Barnacka et al. 2014b). However, the minimum variability time scale of ∼ 1 day observed in these flares constrains the emitting region to $\lesssim 0.01$ pc or $\lesssim 0.001\%$ of the Einstein radius of the lens. In other words, the size of the emitting region is small enough to have a negligible effect on the magnification ratio.

The final issue is $\gamma - \gamma$ absorption. Gamma-ray emission of lensed blazars passes through the lens where low energy photons may absorb the gamma rays of one of the images passing through the more luminous region of lensing galaxy. The absorption may affect gamma-ray photons with energies larger than a few GeV. *Fermi*/LAT detects a majority of photons in the energy range > 100 MeV. In addition, Barnacka et al. (2014a) show that the luminosity of a single galaxy is too low to cause significant absorption of the gamma-ray flux. If all four active periods originated from the same region, absorption would affect all of them in the same way. However, we detect time delays for half of the flaring periods, suggesting that $\gamma - \gamma$ absorption is irrelevant.
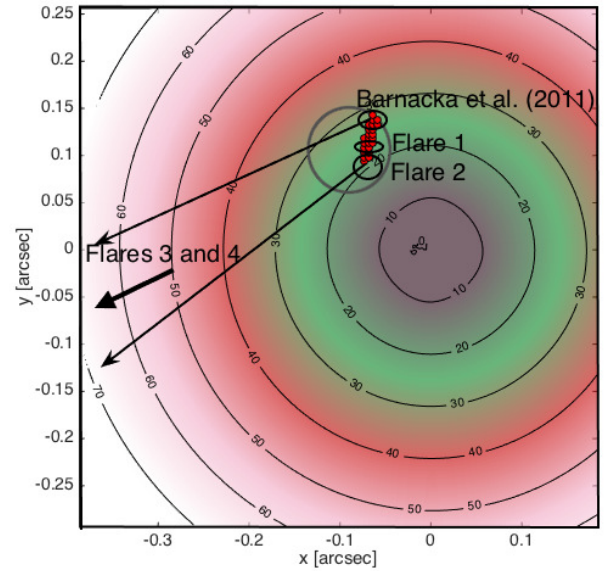


FIG. 17.— Resolved positions of gamma-ray flares. The color pallet and contours indicate the time delays in days. The long arrows show the boundary of the jet alignment limited by well resolved radio observations. Gray circle show the position of the core from Sridhar (2013). Red circles are further constraints on the position of the core using the lens model and the time delay and magnification ratio measurements by Lovell et al. (1998). Ellipses elucidate the spatial origin of the flares obtained through time delay measurement for Flare 1 and Flare 2; they are consistent with the core. The top ellipse shows the spatial origin of the time delay measured by Barnacka et al. (2011) using the gamma-ray light curve in the quiescent state. The short arrow indicates constraints from Flares 3 and 4. The time delays $\gtrsim 50$ days imply that the emitting region must be located at projected distance of $\gtrsim 1.5$ kpc from the core.

A second gravitationally-lensed source, B2 0218+35, shows behavior similar to PKS 1830-211. The bright flaring periods result in time delays consistent with origination from the core. The time delay measured from flaring period at gamma rays is $11.46 \pm 0.16$ days (Cheung et al. 2014). In the radio, Biggs et al. (1999) measured the time delay of $10.5 \pm 0.2$ days and Cohen et al. (2000) obtained a time delay of $10.1 \pm 0.8$ days. However, the most recent gamma-ray flare of B2 0218+35 does not show delayed counterparts suggesting that in this source, flares also have multiple spatial origins.

## 6. CONCLUSIONS

Strong gravitational lensing is a powerful tool for resolving the high energy universe. As a prototypical example of the power of lensing combined with long, uniformly sampled light curves in the gamma-ray regime, we investigate the spatial origin of flares from PKS 1830-211 observed with the *Fermi*/LAT satellite. Despite the poor angular resolution of gamma-ray detectors, gamma-ray flares can be the basis for spatial resolution of a source thanks to the unique observational strategy of the *Fermi*/LAT satellite.

Analysis of four active periods in PKS 1830-211 shows that the gamma-ray radiation during two flaring periods originated from a region spatially coincident with the radio core. The effective spatial resolution we achieve is $\sim 100$ pc.

Two more recent flares apparently do not originate from the core region because the time delay must be $\gtrsim 50$ days. This delay and the lens properties derived from observations at lower energies indicate that these flares must originate at a distance $\gtrsim 1.5$ kpc from the massive black hole powering the blazar. Our analysis demonstrates that variable emission can originate from regions essentially coincident with the core, or from regions substantially displaced along the jet. These flares of short duration originating from regions within the jet challenge our understanding of particle acceleration along with the physical conditions along the jet.

We lay out and apply three methods of time delay estimation from unresolved light curves: (1) the Autocorrelation Function, (2) the Double Power Spectrum, and (3) the Maximum Peak Method. We Monte Carlo simulations to investigate the strengths and weaknesses of these methods and the probability of detecting the gravitationally-induced time delays. We provide details of their application in the appendices.

Monte Carlo simulations demonstrate the power of signal processing (the Double Power Spectrum) in increasing the probability of time delay detection over the more standard autocorrelation methods. The Maximum Peak Method enables us to evaluate the consistency of the detected time delays with the magnification ratios expected from a model consistent with data at shorter wavelengths. For the long active periods consistent with origination in the core, the gamma-ray time delays, $23 \pm 0.5$ days and $19.7 \pm 1.2$ days, are consistent with the radio, $26^{+4}_{-5}$ days.

This analysis lays a foundation for future use of unresolved light curves of lensed sources to enhance the effective angular resolution of the detectors and to elucidate the physics of radiation from distant sources. The *Fermi*/LAT satellite has detected at least one additional lensed blazar which could be analyzed along similar lines. The techniques outlined here can be applied to long-term monitoring data at any wavelength. For example, Euclid, LSST, or SKA, will monitor many distant blazars and we can expect that many of them will be lensed thus enabling a probe of the nature and evolution of radiation from these sources. Long-term, uniformly sampled light curves are the critical input for these signal processing methods.

## REFERENCES

Abdo, A. A., Ackermann, M., Ajello, M., et al. 2010, ApJ, 722, 520

—. 2015, ApJ, 799, 143

Agudo, I., Jorstad, S. G., Marscher, A. P., et al. 2011, ApJ, 726, L13

Atwood, W. B., Abdo, A. A., Ackermann, M., et al. 2009, ApJ, 697, 1071

Barnacka, A. 2013, ArXiv e-prints, arXiv:1307.4050

Barnacka, A., Böttcher, M., & Sushch, I. 2014a, ApJ, 790, 147

Barnacka, A., Geller, M. J., Dell'antonio, I. P., & Benbow, W. 2014b, ApJ, 788, 139

Barnacka, A., Geller, M. J., Dell'Antonio, I. P., & Benbow, W. 2015, ApJ, 799, 48

Barnacka, A., Glicenstein, J.-F., & Moudden, Y. 2011, A&A, 528, L3

Barnacka, A., Moderski, R., Behera, B., Brun, P., & Wagner, S. 2014c, A&A, 567, A113

Bernard, D., Bruel, P., Frotin, M., et al. 2014, ArXiv e-prints, arXiv:1406.4830

Biggs, A. D., Browne, I. W. A., Helbig, P., et al. 1999, MNRAS, 304, 349

Biretta, J. A., Stern, C. P., & Harris, D. E. 1991, AJ, 101, 1632

Bloom, S. D., & Marscher, A. P. 1996, ApJ, 461, 657

Bogert, B. P., Healy, M. J. R., & Tukey, J. W. 1963, in Proceedings on the Symposium on Time Series Analysis, ed. M.Rosenblat, Wiley, NY, 209–243

Bolton, A. S., Treu, T., Koopmans, L. V. E., et al. 2008, ApJ, 684, 248

Böttcher, M., Reimer, A., Sweeney, K., & Prakash, A. 2013, ApJ, 768, 54

Brault, J. W., & White, O. R. 1971, A&A, 13, 169

Burud, I., Magain, P., Sohy, S., & Hjorth, J. 2001, A&A, 380, 805

Chatterjee, R., Bailyn, C. D., Bonning, E. W., et al. 2012, ApJ, 749, 191

Cheung, C. C., Larsson, S., Scargle, J. D., et al. 2014, ApJ, 782, L14

Cohen, A. S., Hewitt, J. N., Moore, C. B., & Haarsma, D. B. 2000, ApJ, 545, 578

Dermer, C. D., Schlickeiser, R., & Mastichiadis, A. 1992, A&A, 256, L27

Edelson, R. A., & Krolik, J. H. 1988, ApJ, 333, 646

Eulaers, E., & Magain, P. 2011, A&A, 536, A44

Eulaers, E., Tewes, M., Magain, P., et al. 2013, A&A, 553, A121

Fassnacht, C. D., Xanthopoulos, E., Koopmans, L. V. E., & Rusin, D. 2002, ApJ, 581, 823

Finke, J. D., & Becker, P. A. 2014, ApJ, 791, 21

Fuhrmann, L., Larsson, S., Chiang, J., et al. 2014, MNRAS, 441, 1899

Garrett, M. A., Nair, S., Porcas, R. W., & Patnaik, A. R. 1997, Vistas in Astronomy, 41, 281

Geiger, B., & Schneider, P. 1996, MNRAS, 282, 530

Giannios, D., Uzdensky, D. A., & Begelman, M. C. 2009, MNRAS, 395, L29

Guirado, J. C., Jones, D. L., Lara, L., et al. 1999, A&A, 346, 392

Gürkan, G., Jackson, N., Koopmans, L. V. E., Fassnacht, C. D., & Berciano Alba, A. 2014, MNRAS, 441, 127

Harris, D. E., Biretta, J. A., Junor, W., et al. 2003, ApJ, 586, L41

Harris, D. E., Cheung, C. C., Biretta, J. A., et al. 2006, ApJ, 640, 211

Harris, D. E., & Krawczynski, H. 2006, ARA&A, 44, 463

Hayashida, M., Madejski, G. M., Nalewajko, K., et al. 2012, ApJ, 754, 114

Hinshaw, G., Larson, D., Komatsu, E., et al. 2013, ApJS, 208, 19

Hirv, A., Olspert, N., & Pelt, J. 2011, ArXiv e-prints, arXiv:1105.5991

Hovatta, T., Petropoulou, M., Richards, J. L., et al. 2015, MNRAS, 448, 3121

Jauncey, D. L., Reynolds, J. E., Tzioumis, A. K., et al. 1991, Nature, 352, 132

Jin, C., Garrett, M. A., Nair, S., et al. 2003, MNRAS, 340, 1309

Jones, D. L., Preston, R. A., Murphy, D. W., et al. 1996, ApJ, 470, L23

Keeton, C. R. 2001a, ArXiv Astrophysics e-prints, astro-ph/0102341

—. 2001b, ArXiv Astrophysics e-prints, astro-ph/0102340

Kochanek, C. S. 2002, ApJ, 578, 25

Koopmans, L. V. E., Treu, T., Fassnacht, C. D., Blandford, R. D., & Surpi, G. 2003, ApJ, 599, 70

Kurtz, M. J., Mink, D. J., Wyatt, W. F., et al. 1992, in Astronomical Society of the Pacific Conference Series, Vol. 25, Astronomical Data Analysis Software and Systems I, ed. D. M. Worrall, C. Biemesderfer, & J. Barnes, 432

León-Tavares, J., Valtaoja, E., Giommi, P., et al. 2012, ApJ, 754, 23

Lidman, C., Courbin, F., Meylan, G., et al. 1999, ApJ, 514, L57

Little, M. A., McSharry, P. E., Roberts, S. J., Costello, D. A. E., & Moroz, I. M. 2007, BioMedical Engineering

Lovell, J. E. J., Jauncey, D. L., Reynolds, J. E., et al. 1998, ApJ, 508, L51

Marscher, A. P. 2012, ArXiv e-prints, arXiv:1201.5402

Marscher, A. P., Jorstad, S. G., Agudo, I., MacDonald, N. R., & Scott, T. L. 2012, ArXiv e-prints, arXiv:1204.6707

Marscher, A. P., Jorstad, S. G., D'Arcangelo, F. D., et al. 2008, Nature, 452, 966

Marscher, A. P., Jorstad, S. G., Larionov, V. M., et al. 2010, ApJ, 710, L126

Marshall, H. L., Schwartz, D. A., Lovell, J. E. J., et al. 2005, ApJS, 156, 13

Martí-Vidal, I., Muller, S., Combes, F., et al. 2013, A&A, 558, A123

Mattox, J. R., Schachter, J., Molnar, L., Hartman, R. C., & Patnaik, A. R. 1997, ApJ, 481, 95

Mattox, J. R., Bertsch, D. L., Chiang, J., et al. 1996, ApJ, 461, 396

Max-Moerbeck, W., Hovatta, T., Richards, J. L., et al. 2014, MNRAS, 445, 428

Meyer, E. T., & Georganopoulos, M. 2014, ApJ, 780, L27

Mücke, A., Protheroe, R. J., Engel, R., Rachen, J. P., & Stanev, T. 2003, Astroparticle Physics, 18, 593

Nair, S., Jin, C., & Garrett, M. A. 2005, MNRAS, 362, 1157

Nakagawa, K., & Mori, M. 2013, ApJ, 773, 177

Nalewajko, K., Begelman, M. C., & Sikora, M. 2014a, ApJ, 789, 161

Nalewajko, K., Sikora, M., & Begelman, M. C. 2014b, ApJ, 796, L5

Nolan, P. L., Abdo, A. A., Ackermann, M., et al. 2012, ApJS, 199, 31

Oguri, M. 2007, ApJ, 660, 1

Oppenheim, A. V., & Schafer, R. W. 1975, Digital signal processing

Pelt, J., Hjorth, J., Refsdal, S., Schild, R., & Stabell, R. 1998, A&A, 337, 681

Pindor, B. 2005, ApJ, 626, 649

Pramesh Rao, A., & Subrahmanyan, R. 1988, MNRAS, 231, 229

Press, W. H. 1978, Comments on Astrophysics, 7, 103

Press, W. H., Rybicki, G. B., & Hewitt, J. N. 1992, ApJ, 385, 404

Ramakrishnan, V., León-Tavares, J., Rastorgueva-Foi, E. A., et al. 2014, MNRAS, 445, 1636

Rathna Kumar, S., Tewes, M., Stalin, C. S., et al. 2013, A&A, 557, A44

Refsdal, S. 1964, MNRAS, 128, 307

Reimer, A., Protheroe, R. J., & Donea, A.-C. 2004, A&A, 419, 89

Roberts, D. H., Lehar, J., & Dreher, J. W. 1987, AJ, 93, 968

Rybicki, G. B., & Press, W. H. 1992, ApJ, 398, 169

Sandrinelli, A., Covino, S., & Treves, A. 2014, A&A, 562, A79

Scargle, J. D. 1982, ApJ, 263, 835

Schechter, P. L., Bailyn, C. D., Barr, R., et al. 1997, ApJ, 475, L85

Sereno, M., & Paraficz, D. 2014, MNRAS, 437, 600

Siemiginowska, A., Bechtold, J., Aldcroft, T. L., et al. 2002, ApJ, 570, 543

Sikora, M., Begelman, M. C., & Rees, M. J. 1994, ApJ, 421, 153

Sikora, M., Janiak, M., Nalewajko, K., Madejski, G. M., & Moderski, R. 2013, ApJ, 779, 68

Sikora, M., Stawarz, Ł., Moderski, R., Nalewajko, K., & Madejski, G. M. 2009, ApJ, 704, 38

Sobolewska, M. A., Siemiginowska, A., Kelly, B. C., & Nalewajko, K. 2014, ApJ, 786, 143

Sridhar, S. S. 2013, Thesis for the Degree of Master of Science in Physics and Astronomy

Stawarz, L., Aharonian, F., Kataoka, J., et al. 2006, MNRAS, 370, 981

Stawarz, Ł., Siemiginowska, A., Ostrowski, M., & Sikora, M. 2005, ApJ, 626, 120

Suyu, S. H., Auger, M. W., Hilbert, S., et al. 2013, ApJ, 766, 70

Tanaka, Y. T., Stawarz, Ł., Thompson, D. J., et al. 2011, ApJ, 733, 19

Tavecchio, F., Ghisellini, G., Bonnoli, G., & Ghirlanda, G. 2010, MNRAS, 405, L94

Tavecchio, F., Maraschi, L., Wolter, A., et al. 2007, ApJ, 662, 900

Tewes, M., Courbin, F., Meylan, G., et al. 2013, A&A, 556, A22

Treu, T., & Koopmans, L. V. E. 2002, MNRAS, 337, L6

Vaughan, S. 2005, A&A, 431, 391

Vaughan, S., Edelson, R., Warwick, R. S., & Uttley, P. 2003, MNRAS, 345, 1271

Wambsganss, J. 2001, in Astronomical Society of the Pacific Conference Series, Vol. 239, Microlensing 2000: A New Era of Microlensing Astrophysics, ed. J. W. Menzies & P. D. Sackett, 351

Wiklind, T., & Combes, F. 1996, Nature, 379, 139

Wiklind, T., & Combes, F. 2001, in Astronomical Society of the Pacific Conference Series, Vol. 237, Gravitational Lensing: Recent Progress and Future Go, ed. T. G. Brainerd & C. S. Kochanek, 155

Winn, J. N., Kochanek, C. S., McLeod, B. A., et al. 2002, ApJ, 575, 103

Wu, X., Su, M., Bravar, A., et al. 2014, ArXiv e-prints, arXiv:1407.0710

APPENDIX

A. SIGNAL PROCESSING IN THE DOUBLE POWER SPECTRUM METHOD

The importance of signal processing has been demonstrated in a wide range of applications including analysis of speech, imaging, or video and seismic events. Signal processing has played a crucial rule in the development of these fields and it is applied extensively in astronomy for spectroscopy, synthetic imaging, and radio astronomy, among others (e.g. XCSAO, Kurtz et al. 1992).

We describe the signal processing method, the Double Power Spectrum, step-by-step. The steps in this signal processing are based on widely used methods (Oppenheim & Schafer 1975; Brault & White 1971). We begin by preparing the light curve, an input time series. For demonstration purposes, we produce an artificial light curve of red noise as a representation of the flaring state. Figure A1 shows (red points) the artificial light curve of red noise of duration 155 units. The green light curve shows the same red noise, but including time delays and corresponding magnification ratios that simulate gravitational lensing of the source. We induced a time delay of 20 days and a

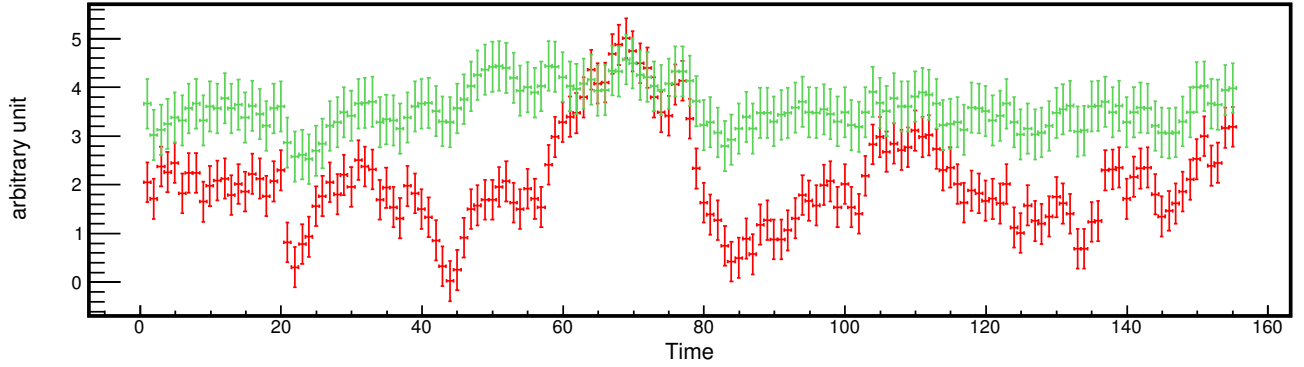magnification ratio of 1.3, following the procedure in Section 3.1.1.



FIG. A1.— Artificial light curves of red noise. The red points represent pure noise. The green light curve is the sum of two components: the first component is the same as the red light curve, and the second component is the identical light curve shifted by 20 days and with an a magnification ratio of 1.3. For visualization purposes, we have added error bars of 20% of the average flux.
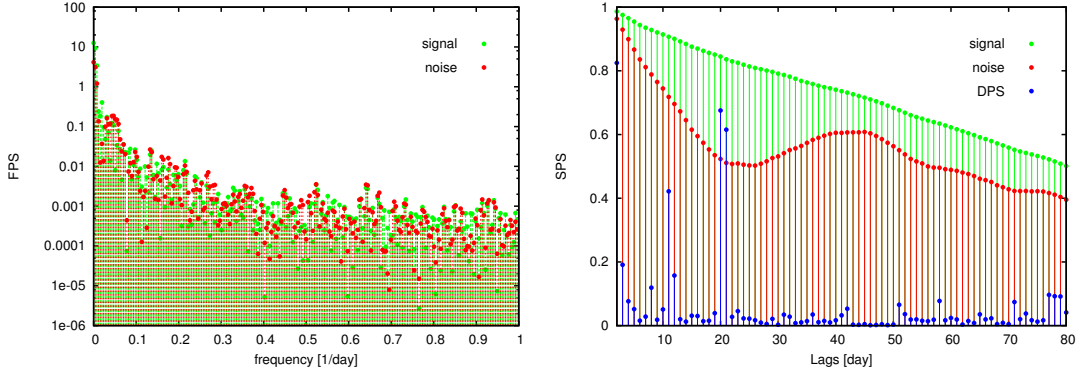


FIG. A2.— No Signal Processing. Right: The First Power Spectrum. Left: The Second Power Spectrum. The SPS is normalized by the maximum values in the spectra. The red points represents the FPS and SPS calculated for the red noise light curve (Figure A1). The green points show the results for the light curve with an artificially induced time delay of 20 days. The blue points in the SPS indicate the result of the full signal processing procedure applied to green light curve that simulates the impact of gravitational lensing.

The DPS method consists of three major stages. The first is a preparation of the input time series, the light curve. The second stage is a calculation of the First Power Spectrum (FPS), and the last stage is a calculation of the Second Power Spectrum (SPS).

Figure A1 shows an example of the light curves, used here as the input. For demonstration purposes, we have used these light curves and calculated the first and second power spectra, without applying any signal processing. Figure A2 shows the result of this analysis with the FPS on the left, and the SPS on the right. Note that the light curve (see Figure A1) serves as an input to the FPS, the FPS is used as an input for the DPS.

The green light curve shows the time series with an artificially induced time delay of 20 days. The DPS for this signal does not show a hint of the time delay detection when there is no signal processing applied. For comparison, in blue, we show the DPS of the same light curve, but after the full signal processing described below.

## A.1. *The First Power Spectrum*

### A.1.1. *Step 1: Removing the Mean and Windowing*

The input time series in the First Power Spectrum is the light curve shown in Figure A1. We start the signal processing by preparing the input. In the first step, we subtract the mean from the time series. This step eliminates the large power in the first bin of the first power spectrum. In the next step, we apply a window function to the input. Windowing is induced to balance the sharpness of the peak of a periodic signal with the spectral resolution. If a time delay is present in the time domain, it will also manifest its presence in the frequency domain (the FPS) as a periodic pattern with a period inversely proportional to the time delay (see equation (4)). Thus, we must preserve the maximum resolution of the FPS; for this purpose, we use a rectangular window.

### A.1.2. *Step 2: Zero Padding*

To avoid the large power at low frequencies caused by discontinuity at the beginning and the end of the time series, we apply zero padding to the time series.
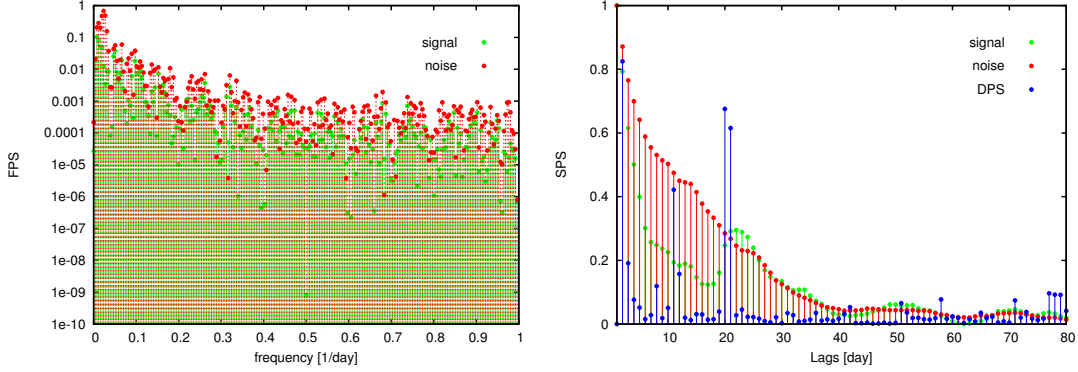


FIG. A3.— Right: The First Power Spectrum. Left: The Second Power Spectrum. The input to the FPS are light curve in Figure A1 after applying Steps 1,2 and 3 of the FPS signal processing. The input to the DPS is the FPS without any signal processing. The colors are the same as in Figure A2.

### A.1.3. *Step 3: Doubling the Points*

Next, to avoid aliasing, we double the points. Doubling the points does not introduce additional signal, but, it shifts the Nyquist frequency and therefore allows the power of the spectrum to go to zero when the frequency approaches the Nyquist frequency. We apply the Fourier transform and calculate the power spectrum of the time series.

Figure A1 shows the results of these steps of signal processing. The time delay in the green light curve appears as a broad peak around the true value of simulated time delay.

### A.2. *The Second Power Spectrum*

The resulting FPS (see Figure A3, left) serves as an input for the SPS. We again process the input before applying the Fourier transform.

### A.2.1. *Step 1: Flattening and Mean Extraction*

The observed light curve of blazars can be characterized by power law noise. This type of signal has large power at low frequencies and thus the signal is not stationary (there is a trend in the data). To "flatten" the signal, we take the logarithm of the power spectrum (Bogert et al. 1963). Then we can remove the part of the spectrum at low frequencies with large amplitude resulting from power law noise. Next, we remove the average from the series. Figure A4 (left) shows the input and and the corresponding power spectrum is shown on the right. These steps successfully reduce the high amplitudes at short (and spurious) time delays and sharpen the peak around the true time delay.
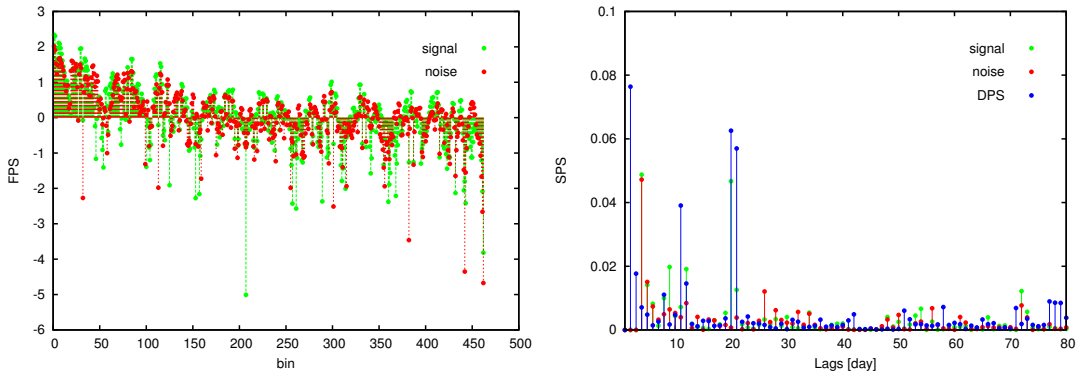


FIG. A4.— Right: The First Power Spectrum. Left: The Second Power Spectrum. The spectra are calculated after applying signal processing to the light curve, and then processing the FPS by flattening the spectrum and removing a mean (Section A.2.1).

In the SPS, the signal of interest is characterized as a peak around the true value of the time delay. Thus, successful processing should sharpen the peak. Here we use the Bingham window[2], a combination of a rectangular and a Hanning window.
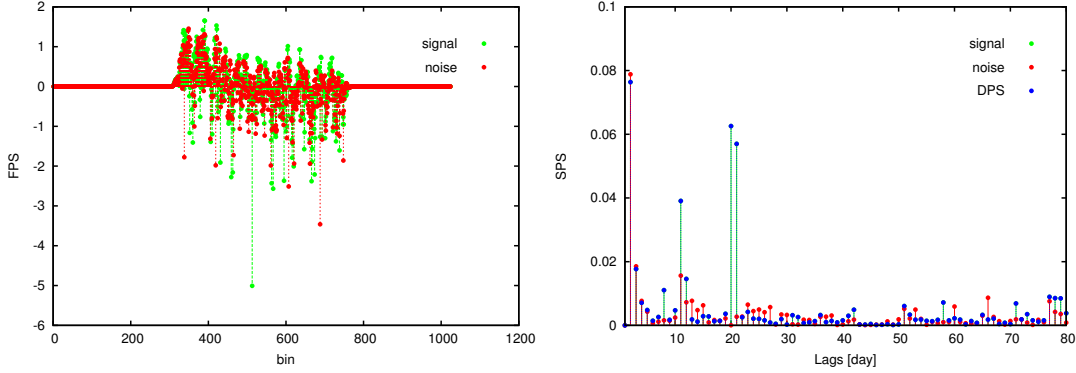


Fig. A5.—  Right: First Power Spectrum. Left: Second Power Spectrum. Results obtained after applying the full signal processing.

Finally, we apply zero padding to the signal and calculate the final SPS (see Figure B3). Monte Carlo simulation demonstrate the effectiveness of the signal processing we have applied. Figure B3 displays the results for one possible realization of the light curve. The DPS method is efficient in detecting time delays independent of the character of the signal (whether the light curve is white or red noise) and the method is also very resistant to producing spurious detection of time delays even in very structured time series of red noise.

## B.  MAXIMUM PEAK METHOD - SIMULATIONS

The time series of gamma-ray light curves consist of short duration flares with variability time scales on the order of hours to days. We can use this characteristic of the time series to identify the most prominent flares in the light curves; we calculate the ratio between the flux during the flare and the flux in the successive bins. The resulting flux ratio is a proxy for the magnification ratio.

The mirage image arriving first has a larger magnification than the echo images. Thus, the most luminous flares can be associated with the first mirage image. The echo flares should appear with a flux diminished by a factor corresponding to the magnification ratio. Thus we can look for time periods (time bins) when the flux ratios (normalized to brightest flares) are consistent with the magnification ratios predicted for a particular projection of the jet and lens model.

The active periods may consist of a series of flares (Flare 1 and Flare 2), or they can consist of a single outburst (Flare 3 and Flare 4). Analysis of light curves containing single flares is difficult because of the low photon statistics before and after the flare. Thus the light curve calculated for short time bins may consist primarily of upper limits. Such light curves are useless for the Autocorrelation Function, or even for the Double Power Spectrum methods. However, light curves containing single isolated flares can still reveal the echo flares and their time delays and magnification ratios. We demonstrate the Maximum Peak Method applied to a single simulated flare in Section B.1.

Long active periods with good photon statistics allow construction of gamma-ray light curves where only a small fraction of the bins have upper limits only. These light curves are perfectly suited for methods like the Autocorrelation Function and the Double Power Spectrum. In this case, the Maxim Peak Method is a powerful consistency check if the detected time delays are consistent with the parameters predicted by lens model. We demonstrate the performance of this method on simulated superimposed series of flares in Section B.2.

The Maximum Peak Method is complementary to the Autocorrelation Function and the Double Power Spectrum in the search for gravitationally-induced time delays in unresolved flaring light curves.

### B.1.  *Single Flares*

Flare 3 and Flare 4 are single isolated outbursts. We base our simulations on Flare 3.

Flares are observed when the emission significantly exceeds the level typical of the quiescent state. For single isolated flares the emission before and after the flare is consistent with the average flux. Therefore, the average flux originates from the site of quiescent emission. The temporal behavior of quiescent emission is accurately represented by pink noise. We thus start our Monte Carlo simulations by producing light curve composed of pink noise. The flaring episode with a flux increase by a factor of 5 is inconsistent with pink noise. We add a flare to the light curve with a time structure and flux per each bin similar to Flare 3. Then we introduce an echo flare with a time delay of 48 days and magnification ratio 4.5 (Figure B1, green points). The choice of these parameters relays on the results of the Maximum Peak Method for Flare 3. We also simulate an echo flare with time delay of 23 days and magnification ratio

---

[2] http://www.vibrationdata.com/tutorials/Bingham_compensation.pdf

1.8 (Figure B1, red points). We simulate the echo flare at 23 days to demonstrate that if the flare would originate from the region consistent with the core then the echo flare would be detectable.
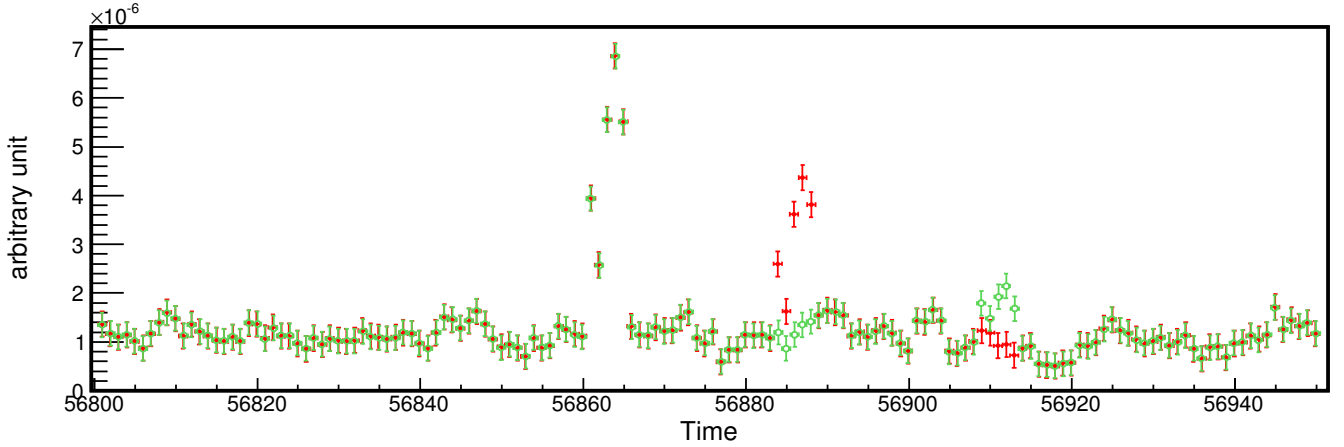


FIG. B1.— The artificial light curve generated as pink noise with a flare like structure with time delay of 48 days. This light curve simulates Flare 3. We include an echo flare with a time delay of 48 days and magnification ratio of 4.5 (green points). Red points represent the light curve with an echo flare at a time delay of 23 days and magnification ratio of 1.8.

Figure B3 shows the result of applying the Maximum Peak Method to the simulated light curve shown in Figure B1. The method shows that the ratio we obtain between the flux of the flare peak and the flux in the bin corresponding to echo flare agree with model predictions. The method rejects the majority of time delay ranges where there is no consistent magnification ratio.
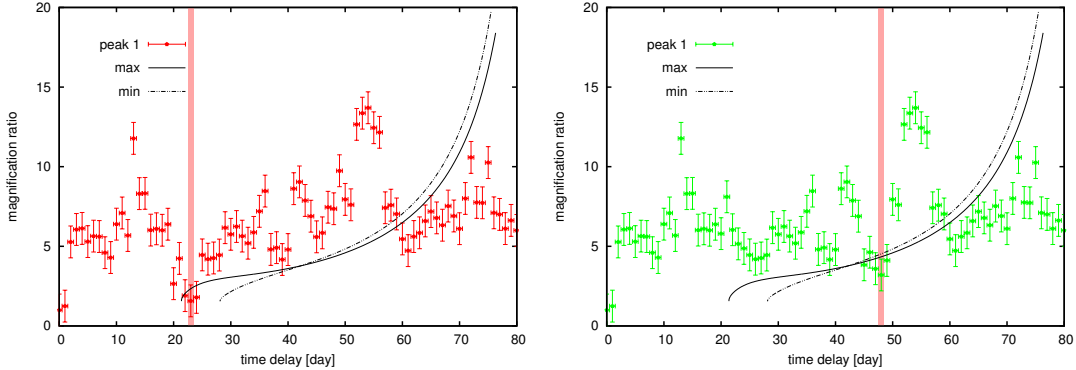


FIG. B2.— Maximum Peak Method applied to the simulated light curve Figure B1. The red area indicates the time bin corresponding to the simulated time delay. Solid and dashed lines indicate the model predictions for magnification ratio as a function of the time delay for boundary alignments of the jet constrained by the radio observations (Figure 2). Left: Results for simulated light curve with induced echo flare with time delay of 23 days and magnification ratio 1.7. Right: Simulated light curve with induced time delay of 48 days and magnification ratio 4.5

Note that the maximum distance of the emitting region along the jet which we can constraint depends on the ratio between the observed flux of the flare and the flux relative to quiescent state. Flare 3 and the simulated flare exceed the average flux by a factor of $\sim 5$. In this example, if the predicted magnification ratio is larger than $\sim 5$, we do not expect to be able to detect the echo flare; the flux of the echo flare is then below the average of the quiescent state. Thus, we can only test expected magnification ratios for Flare-3 in the range from 1 to 5.

For Flare-3 the magnification ratio $\sim 5$ corresponds to a region along the jet located at least 1.5 kpc from the core (see Figure 3). Detection of a consistent magnification ratio $f \sim 5$ still does not provide clear evidence of echo flare detection because the data are also consistent with a flare from a region at distances $\geq 1.5$ kpc from the core. In other words, the observed magnification ratio sets a very interesting limit on the distance between the core and the origin of the flare, but it does not pinpoint it location.

### B.2. *Superimposed Series of Flares*

Here we investigate the performance of the Maximum Peak Method applied to a light curve which consists of a series of superimposed flares. Flares 1 and 2 are examples. As an input time series we use the simulated light curve shown in Figure A1.

Figure B3 shows the result of the Maximum Peak Method applied to the series of superimposed flares. The method confirms that the time delay detected with Double Power Spectrum is consistent with the predictions and the method excludes significant ranges of possible time delays.
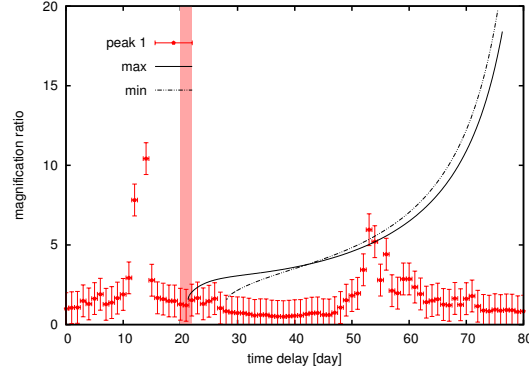


FIG. B3.— Maximum Peak Method applied to the simulated light curve shown in Figure A1.